REVISION 2

A revisit to phase transition behavior of K-feldspar at high-pressure and high-temperature: Implications on metastable K-feldspar in cold subduction

Chengcheng He[1,2] · Heping Li[1*]

1 Key Laboratory of High-temperature and High-pressure Study of the Earth's Interior, Institute of Geochemistry, Chinese Academy of Sciences, Guiyang, 550081, China

2 University of Chinese Academy of Sciences, Beijing, 100049, China

* Corresponding author: liheping@mail.gyig.ac.cn

Abstract

Felsic gneiss is main type of ultrahigh-pressure metamorphic rocks in continental subduction zones. As one of the important mineral of felsic gneiss, the phase behavior of K-feldspar is of great significant to study subducting seismic activities, crust-mantle interactions and plate tectonics in the Earth's interior. Thus, the phase relations in K-feldspar are constrained by Raman spectroscopy combined with externally-heating diamond anvil cell (DAC) under high-pressure (28 GPa), high-temperature (400 ℃), and simultaneous high pressure-temperature (*P-T*) (14 GPa, 430 ℃) conditions. The phase diagram of K-feldspar at relatively lower temperature has been complemented, and a more comprehensive *P-T* phase diagram of K-feldspar is established along with previous results. K-feldspar undergoes a reversible phase transition from *C-1* to *P-1* (metastable K-feldspar) symmetry at 10.3 GPa. Metastable K-feldspar is an intermediate phase from K-feldspar to K-holl-I ($KAlSi_3O_8$ with a hollandite-I structure) in extremely cold subduction slabs (<2℃/km) or the center of some old, cold, and rapidly subducting slabs. Metastable K-feldspar is stable even at 11.4 GPa and 400℃ in enriched hydroxyl group (OH) environments, which shows greater high *P-T* stability than K-feldspar. So metastable K-feldspar could withstand subduction-zone fluids low-temperature metamorphism and survive to deeper than previously expected. This study enhances our understanding of the formation paths and conditions of K-holl-I, the subducted depth of K-feldspar, the effect of subduction-zone fluids on continental subduction, and provides a possible reason for the origin of intermediate- and deep-focused seismicity.

Keywords: metastable K-feldspar, Raman spectroscopy, high pressure-temperature conditions, continental subduction, subduction-zone fluids

Introduction

Feldspar minerals comprise about 50-60% of the Earth's crust and are widely found in the surface of other planets (e.g., Moon, Mars, Venus) (Sprague et al. 1997; Rogers and Nekvasil 2015; Hashimoto et al. 2009). K-feldspar (microcline, sanidine, orthoclase; $KAlSi_3O_8$) is more stable than other two principal rock-forming end-members (albite, anorthite), and has been regarded as a predominant potassic phase in the Earth's crust and the uppermost mantle (e.g., Liu et al. 2010; Deng et al. 2011). In addition, K-feldspar could enter the deep Earth via subduction process, crustal constituents are directly transferred from the descending slab into the mantle wedge at different depths, leading to the crust-mantle interaction (Irifune et al. 1994; Zhang et al. 2003; Zheng 2012). Furthermore, K-holl-I is regarded as a host phase for large cations such as K, Na, Sr, Ba, and Pb in the mantle, which is of great geochemical interest (e.g., Yamada et al. 1984). Thus, the stability of K-feldspar is of great geophysical and geochemical significance to understand the dynamics of subducting lithospheres, Earth's long-term thermal evolution, and the material exchange of the crust-mantle system.

The framework of K-feldspar is based on the rings of four TO_4 tetrahedra (T = Si^{4+}, Al^{3+}) forming double crankshaft-like chains. All Si and Al atoms are bonded to four O atoms in the TO_4 tetrahedra, and potassium atoms occupy the large voids. K-feldspar dives into the Earth interior along with a series of structural and compositional changes. Phase equilibrium experiments confirmed that at temperatures above 700 °C, K-feldspar dissociated into a denser assemblage of $K_2Si_4O_9$ wadeite +

kyanite + coesite/stishovite (Wd + Ky + Coe/St) at 6-7 GPa, and latter the assemblage recombined into K-holl-I at 9-10 GPa (e.g., Urakawa et al. 1994; Yagi et al. 1994; Liu et al. 2010). K-holl-I transformed into K-holl-II ($KAlSi_3O_8$ with a hollandite-II structure) at near 20 GPa, both ambient and elevated temperatures. K-holl-II is unquenchable and stable over the entire range of mantle conditions (Sueda et al. 2004; Nishiyama et al. 2005; Ferroir et al. 2006; Hirao et al. 2008); In addition, K-feldspar melted to leucite ($KA1Si_20_6$) and silica-rich liquid at 2 GPa, 1150 ℃ (Lindsley 1966), and transformed into metastable phase induced by an increase in the Al coordination number at 10-13 GPa and ambient temperature (Pakhomova et al. 2020).

Metastability of subducted minerals could encourage subducting slabs deceleration or stagnation (e.g., Van Mierlo et al. 2013; Agrusta et al. 2014). It is well known that low-temperature parts in the Earth's subduction zones enable the preservation of metastable phases at greater depths than those under equilibrium conditions (e.g., Hogrefe et al. 1994; Kawakatsu and Yoshioka 2011). However, previous high *P-T* studies of K-feldspar are insufficient to be applied to in the ultracold subducted environments, and the lower temperature parts (below 700 °C) of the phase diagram has not be carefully investigated yet. Besides, Pakhomova et al. (2020) studied the stability of metastable albite and anorthite by quenching experiments, and proposed anorthite may exist at deeper depths than expected in the Earth's interior. As one of the important mineral of felsic gneiss, the high *P-T* stability of metastable K-feldspar is also worthy of attention. Herein, the phase relations at relatively low temperature of K-feldspar are investigated firstly by Raman

spectroscopy in externally-heating DAC under high-pressure (28 GPa), high-temperature (400 ℃), and simultaneous high *P-T* (14 GPa, 430 ℃) conditions. We also presented the isothermal (γ_{iT}) mode Grüneisen parameters, isobaric (γ_{iP}) mode Grüneisen parameters, and intrinsic anharmonic mode parameters of K-feldspar. Besides, a series of ex situ multi-anvil experiments were performed to clarify the high *P-T* stability of metastable K-feldspar. This study complements the gap in the phase diagram of K-feldspar at relatively low temperature, and a more comprehensive *P-T* phase diagram of K-feldspar is established along with previous studies. The results provide new insights into the phase behavior of K-feldspar in subduction zone at different thermal gradients (especially at the ultracold), and the possible seismicity caused by their intruding plates (Zheng 2019).

Material and Methods

Sample synthesis and characterization

High-purity K-feldspar was synthesized by solid-state reaction. Reagent-grade $KHCO_3$, Al_2O_3 and SiO_2 powders were mixed in a molar 2:1:6 ratio. The powder mixtures were crushed with ethanol in an agate mortar for 1 h, and then placed in a Pt crucible and heated up to 800 ℃ in a stove for 12 h to ensure a sufficient decarbonation. The recovered mixture was ground finely and then pressed into pellets with diameter of 6 mm and length of 3 mm under uniaxial pressure of 4 MPa. High *P-T* synthesis experiment was performed on DS 6 × 600 t cubic-anvil-type apparatus at the Key Laboratory of High-Temperature and High-Pressure Study of the Earth's

Interior, Institute of Geochemistry, CAS, Guiyang, China. Figure 1 (a) shows a schematic of the cross section of the experimental assemblage. A pellet was covered by the silver foil of 0.025 mm thickness, pyrophyllite cube (32.5 mm × 32.5 mm × 32.5 mm) and h-BN were applied as the pressure medium, and a graphite was used as the heater at 1.8 GPa, 900 ℃ for 2 h. The pressure was reduced to ambient conditions after quenching. The reactant was confirmed as a K-feldspar single phase by both powder X-ray and Raman spectrum, as Figures 1 (b-c) shown.

In situ high-pressure and high-temperature Raman experiments

The Raman spectra of synthetic K-feldspar under high-pressure (up to 28 GPa) and room-temperature, high-temperature (up to 400 ℃) and ambient-pressure, and simultaneous high *P-T* conditions (up to 14 GPa, 430 ℃) were collected in DAC. The sample chambers were firstly compressed up to target pressures, and then heated. High-pressure conditions were generated by a pair of 400 mm diamond culets. The 250-μm-thick rhenium gaskets were pre-intended to dense disks of ~60 μm thickness, and then drilled a hole as the sample chamber with a diameter of ~160 μm. The 4:1 mixture of methanol-ethanol (ME), 16:3:1 mixture of methanol-ethanol-water (MEW), helium, nitrogen or ultrapure water (H_2O) were selected as pressure-transmitting mediums (PTMs). The gaseous PTMs were loaded by a high-pressure gas-loading apparatus sealed at above 0.4 GPa. The gas-loading apparatus is developed in the Sanchez Technologies and located at the Key Laboratory of High-Temperature and High-Pressure Study of the Earth's Interior, Institute of Geochemistry, CAS, Guiyang,

China. High-temperature environments were achieved by two external electric NiCr resistance heating furnace in series around the diamonds. Temperatures were measured by a R/S type platinum–rhodium and platinum thermocouple (Omega technology company, America) with the precision of ±1 ℃ in our experimental temperature range. The thermocouple was used for temperature measurement and stabilization through a feedback loop in the temperature controller (CN3251,Omega technology company). Every time before the Raman spectrum was collected, we kept the temperature at least 5 min to guarantee the stabilization and uniformity of temperature in the sample chamber. The R1 line of tiny ruby (Cr^{3+} doped α-Al_2O_3) spheres and 0-0 line of SrB_4O_7:Sm^{2+} grains (synthetic method was described in previous study) (Mao et al. 1986; Zhao et al. 2017) were selected to calibrate pressure at high-pressure and high *P-T* experiments, respectively. Compared to Ruby, the 0-0 line of SrB_4O_7:Sm^{2+} presents very small temperature response, including frequency shift and broadening. So it is the preferred pressure calibration under high *P-T* conditions. The spectra of the calibrator were measured at each pressure before and after sample data collection, and the average pressure values were taken. The Raman spectra were collected at a confocal Renishaw in Via Raman Microscope in the Key Laboratory of High-Temperature and High-Pressure Laboratory Institute of Geochemistry, Chinese Academy of Sciences, Guiyang. The tilting and rotation of the spectrometer relative to the incident laser beam were calibrated using a silicon wafer with a static spectrum centered at 520 cm^{-1}. Samples were excited by an Argon ion laser (λ = 514.5 nm) operated at 20 mW with a focused laser spot of ~5 μm in

diameter through a SLM Plan 50 × Olympus microscope objective. A spectrometer with a liquid nitrogen-cooled CCD detector was used to collect the Raman data. The accurate peak positions of the Raman spectra were fitted by *PeakFit* software.

Multi-anvil experiments

The high *P-T* conditions of quenching experiments were provided using a 1000-ton Kawai-type multi-anvil apparatus at the Key Laboratory of High-Temperature and High-Pressure Study of the Earth's Interior, Institute of Geochemistry, CAS, Guiyang, China. The sample assembly was displayed in Figure S1. Eight tungsten carbide cubes with a truncation of 6 mm were used as second-stage anvils, and a Cr_2O_3-doped MgO octahedron with edges of length of 14 mm was used as pressure medium. Starting materials were the high-purity K-feldspar synthesized in this study. Graphite sleeve, platinum closure column, MgO tube, ZrO_2 tube and Al_2O_3 plug were used as the heater, the sample capsule, the insulator, and the thermal insulation sleeve, respectively. The temperature was measured using a $W_{95}Re_5$-$W_{74}Re_{26}$ thermocouple inserted axially under the sample capsule. To remove absorbed water, all parts composed of MgO, Al_2O_3, or ZrO_2 were baked at 1000 ℃ for 1 h before the experiments. The sample chambers of three quench experiments were firstly compressed up to 15 GPa, and then heated to 500 ℃, 650 ℃, and 800 ℃ at a rate of 20 ℃/min, respectively. The duration time at each target temperature was at least 2 h before rapid quenching.

Results and Discussion

Raman spectrum of K-feldspar at ambient conditions is presented in Figure 1 (b). 12 modes of the 39 Raman modes ($20A_g + 19B_g$) predicted by factor group analysis (Tseng et al. 1995) were observed. The strongest triplet peaks at 451.98, 475.44, and 512.98 cm^{-1} (denoted as I_a, I_b, I_c modes) are ascribed to the ring-breathing of the four-membered rings of tetrahedra. Three Raman peaks at 117.23, 156.34, and 195.19 (expressed as III_a, III_b, III_c modes) are assigned to cage-shear. Two peaks at 282.91 and 403.21 cm^{-1} (named as II_a, II_b modes) are due to the rotation–translation of the four-membered rings. Two weak modes at 758.76, 803.59 cm^{-1} (marked as IV_a and IV_b modes) are attributed to the deformation of the tetrahedra. The broad peaks with position at around 1023.44 and 1118.38 cm^{-1} (labeled as V_a and V_b) belong to the vibrational stretching modes of the tetrahedra. Most Raman modes coincide well with previous studies, except for the modes of IV_a, IV_b, V_a and V_b due to the weak intensity (Freeman et al. 2008; Bendel and Schmidt 2008; Peterson et al. 2009; Befus et al. 2018). The slight differences in wavenumber for observed modes may result from the synthetic environment, peak overlap, and orientation dependence.

Raman spectroscopy of K-feldspar at high-pressure/high-temperature

High-pressure Raman spectra of K-feldspar were collected up to 28 GPa at room temperature, and were only studied in the spectral range 100-800 cm^{-1} due to the intense Raman bands of MEW at 880-1200 cm^{-1}. The typical high-pressure Raman spectra are showed in Figure 2 (a). At high pressure, a general deterioration of the

Raman signal and amorphization effect can be observed. I_b, I_c, II_a, III_b modes can be distinguished clearly within 10 GPa, while only the strongest mode I_c can be observed clearly within the entire studied pressure range. All the Raman modes shift to higher wavenumbers with increasing pressure because of the TO_4 tetrahedra shrinkage and the stronger electrostatic repulsion. The corresponding pressure shifts and the full width at half maximum (*FWHM*) of I_c mode are plotted in Figures 2 (b-c), from which two obvious inflection points at 6.5 GPa and 14.7 GPa can be observed, and another obvious inflection point at 10.3 GPa can been seen in Figure 2 (c). The pressure coefficient ($\partial v_i/\partial P$) changes from 3.72(2) to 3.07(9) $cm^{-1}GPa^{-1}$ at the first discontinuity point (at 6.5 GPa). However, X-ray diffraction (XRD) studies reported microcline experienced a continuous compression up to 7 GPa, then underwent an elastic softening with an increase of the *a*-axis and a decrease of the *b*-axis at 7-9 GPa; meanwhile, the α and β unit-cell angles rapidly increased while the γ unit-cell angle decreased at pressures above 6.7 GPa (Allan and Angel 1997; Pakhomova et al. 2020). Thus, the first discontinuity point at 6.5 GPa could not be ascribed to a phase transition but the change in compressional mechanism at atomic scale, which result in the elastic behaviour change. Similar discontinuity was also found in the isostructural mineral, low albite, at 6.5 GPa (Aliatis et al. 2017). The wavenumbers of I_c mode change linearly upon further compression from 6.1 to 14.2 GPa, wheras the *FWHM* shows an abrupt change at ~10.3 GPa. Similar discontinuity was also found in low albite at 8.5 GPa with the $\partial v_i/\partial P$ of the mode at 815 cm^{-1} (corresponding to IV_b modes) showing a discontinuity (Aliatis et al. 2017). Pakhomova et al. (2020) reported a

displacive phase transition of K-feldspar from *C-1* to *P-1* (metastable phase) symmetry, which was induced by an increase in the Al coordination number from four to six upon 10.4-12.8 GPa. Thus, we infer the second discontinuity at 10.3 GPa is relate to the phase transition from K-feldspar to metastable phase. The accurate phase transition range is 9.7 to 10.8 GPa. An additional Raman experiment up to 13 GPa demonstrated the reversibility of the phase transition (Figure S2 (a)). The third discontinuity at 14.7 GPa is relate to the solidification of MEW which caused an irreversible pressure-induced amorphization. The high-pressure behaviour of feldspars is highly sensitive to deviatoric stress. Previous study reported metastable K-feldspar was stable at least up to 27 GPa in hydrostatic conditions (Pakhomova et al. 2020). While in this study, the *FWHM* of I_c mode increased and the intensity decreased rapidly at above 14.7 GPa. Upon further compression at above 23.1 GPa, sample was fully amorphous and remained amorphous structure on recovery to ambient conditions. Another high-pressure Raman experiment in H_2O up to 20.4 GPa indicated the reversibility of the not fully amorphization (Figure S2 (b)). Previous results about the pressure-induced phase transition of feldspars at room temperature reported a displacive phase transition occurred for both anorthite and oligoclase at 2.2-3.9 GPa, accompanied by the occurrence of a new peak near the *Ic* mode, which was mainly caused by the reduction of Ca-O bond length (Xie et al. 2012; Pakhomova et al. 2020). However, the phase transition behavior was not found in K-feldspar and albite during the compressing processes (Aliatis et al. 2017; Pakhomova et al. 2020). We infer the phase behavior at relative low pressure of feldspars is significantly affected by the

(Ca,Na,K)-O bond length and bond energy. Moreover, the three end-members all experienced a coordination number increase of Al atoms to further adapt to the high-pressure conditions (Pakhomova et al. 2020).

High-temperature Raman spectra of K-feldspar were collected up to 400 ℃ at ambient pressure. The typical high-temperature Raman spectra are showed in Figure 3 (a), and the variation of Raman shift at different temperatures is plotted in Figure 3 (b). The Raman shifts of all observed bands for K-feldspar continuously decrease with increasing temperature, and no phase transition was observed during heating in this study, which was consistent with previous studies (Henderson 1979; Hovis et al. 2010). Generally, the Raman peaks shift slightly to lower frequency regions with increasing temperature because of the longer bond length and weaker bond. Changes of *FWHM* and signal intensity of Raman peaks under high-temperature conditions are not great as that under high-pressure conditions (i.e., increase of *FWHM* is ~4.7 cm^{-1} for I_c mode in the investigated temperature range).

Combined the Raman spectra of K-feldspar under high-pressure and high-temperature conditions, the pressure coefficients ($\partial v_i/\partial P$) and the temperature coefficients ($\partial v_i/\partial T$) of observed Raman bands are listed in Table 1 and Figure S3. The Raman modes could be seen approximately as continuous increases within ~10.3 GPa. The pressure coefficients of Raman vibrations of K-feldspar vary from 1.41 to 5.32 $cm^{-1}GPa^{-1}$, and the temperature coefficients vary from -0.17×10^{-2} to -0.82×10^{-2} $cm^{-1}K^{-1}$. The modes relate to the rotations of the four non-equivalent tetrahedra and the translation of K^+ cations (e.g., III_a, III_b, Aliatis et al. 2015) show the biggest

266 change in slope with pressure and temperature. The isothermal (γ_{iT}) and isobaric (γ_{iP})
267 mode Grüneisen parameters are important physics quantities to describe the elasticity
268 and anharmonicity under high *P*-*T* conditions, which can be calculated by the
269 following equations and are listed in Table 1 (Gillet et al. 1989):

270 $$\gamma_{iT} = (K_T / \nu_{i0})(\partial \nu_i / \partial P))_T \quad (1)$$

271 $$\gamma_{iP} = -(1/\nu_{i0}\alpha)(\partial \nu_i / \partial T)_P \quad (2)$$

272 where v_i is the Raman shift of the *i*-th vibrational mode, v_{i0} is the frequency of mode v_i
273 at 0 GPa, K_T is the isothermal bulk modulus with value of 58.3 GPa (Allan and Angel
274 1997), α is the volume thermal expansion coefficient with value of 1.44×10^{-5} K^{-1}
275 (Henderson, 1979), defined as $\alpha = (1/V)(\partial V / \partial T)_P$. The calculated values of γ_{iT}
276 range from 0.26 to 1.96, and γ_{iP} change from 0.41 to 4.51. The average γ_{iT} value of
277 Raman modes of tetrahedra (0.32) are much smaller than that of the tetrahedral cages
278 (1.96), and the thermal expansion differs more with a smaller average γ_{iP} value of
279 tetrahedra (0.61) and a larger average γ_{iP} value of the tetrahedral cages (3.42). The
280 average γ_{iT} and γ_{iP} values are small for the TO_4 tetrahedra, which reflects their relative
281 incompressibility and weak expansivity. Hence, the weaker bonds (K-O) are affected
282 more by increasing pressure and temperature. It is obvious that the tetrahedra are
283 much more incompressible than the tetrahedral cages, which is consistent with other
284 feldspars (e.g., oligoclase from Xie et al. 2012). The γ_{iP} are different with the γ_{iT} for
285 same mode, which means an intrinsic anharmonicity. The intrinsic anharmonic mode
286 parameter βi can be calculated by the following equation and are listed in Table 1:

287 $$\beta_i = \alpha(\gamma_{iT} - \gamma_{iP}) \quad (3)$$

288 the obtained β_i change from -0.46×10^{5} to -0.16×10^{-5} K^{-1}, with an average of
289 -0.26×10^{-5} K^{-1}.

290

291 **Raman spectroscopy of K-feldspar at simultaneous high *P-T* conditions**

292 Raman spectra of K-feldspar in different PTMs were collected at pressures up to
293 14.7 GPa and temperatures up to 430 ℃ (Figure S4). During heating at a certain
294 initial pressure, the real pressure of sample chamber changed because of thermal
295 expansion and stress relief of experimental materials. Thus, we measured the pressure
296 of sample chamber by the fluorescence spectra of $SrB_4O_7:Sm^{2+}$ in real-time. The
297 representative Raman spectra of K-feldspar obtained under simultaneous high *P-T*
298 conditions are presented in Figure 4. Given the 4:1 ME mixture can conveniently
299 provide a hydrostatic condition at below 10.5 GPa (Klotz et al. 2009), and has
300 relatively simple ingredients, it was firstly selected as the PTM. At first initial
301 pressure points of 1.8 GPa, with temperature increasing, no any meaningful variation
302 except pressure- and temperature-induced frequency shifts were observed (Figure S4
303 (a)). With further compressing and heating, the peak shape changed firstly at 400 ℃
304 and 5.9 GPa with a new peak appearing at ~430 cm^{-1}, and the Raman shift of mode at
305 ~290 cm^{-1} clearly showed a discontinuous evolution (Figure S4 (b)). Then the
306 variation became apparent at 400 ℃ and 6.7 GPa with several new peaks at 206, 215,
307 357, 392, 430, and 465 cm^{-1}, while some new peaks disappeared after further heating
308 (Figure S4 (c)). We even observed some bubbles welling up in the sample chamber,
309 but it was hard to record and measure because of its quick breaking. Similar Raman
310 spectra variation were also observed at *P-T* range of 350-430 ℃ and 7.3-8.1 GPa
311 (Figure S4 (d)), while surprisingly did not appear at 11.4-13.9 GPa (Figure S4 (e)).

312 The new peaks revealed at least one reaction occurred. Due to the signal-to-noise ratio
313 deterioration and the Raman peaks broadening under high *P-T* environments, it was
314 difficult to identify the new phase via the ambiguous peaks. Luckily, the new peaks
315 sharpened and the shape of the main strong peaks remain unchanged during cooling
316 and decompressing periods (Figure S5), which made the recovered sample easy to
317 distinguish, and could be referred to the high *P-T* new phase. Raman spectra of
318 samples recovered from high *P-T* to ambient conditions in different PTMs are shown
319 in Figure 5. The Raman spectrum of recovered sample from 430 ℃, 6.7 GPa (ME) in
320 Figure 5 is virtually same as that in Figures S4 (b-d), and it is consistent well with the
321 characteristic peaks of an assemblage of coesite, stishovite and $KHCO_3$ (Figure S6
322 (a)). Besides, we accidentally conducted another experiment at 4.7-5.9 GPa,
323 20-400 ℃ in the 16:3:1 MEW mixtures (Figure S4 (f)), and the Raman spectrum of
324 recovered sample can be indexed to coesite and muscovite (Figure S6 (b)). However,
325 because of the appearance of coesite, and the reaction did not occurred in the *P-T*
326 range of 1.8-3.2, 11.4-13.9 GPa and 20-400 ℃ (Figures S4 (a) and S4 (e)), it was
327 difficult to confirm whether the ME/MEW mixtures reacted with K-feldspar or with
328 its phase transition products, such as wadeite-type $K_2Si_4O_9$ (Wd). In order to further
329 study the stability of K-feldspar under high *P-T* conditions, we replaced the PTM. We
330 conducted two high *P-T* experiments in helium and in no PTM, respectively (Figures
331 S4 (g-h)), and found K-feldspar was stable at the experimental *P-T* range.
332 All up, pure K-feldspar is stable and does not decompose to an assemblage of Wd
333 + Ky + Coe/St within the *P-T* range (0-11.4 GPa, 20-430 ℃) in this study.

Nonetheless, if fluid components added, the stability of K-feldspar is different. The results of in situ Raman experiments under high *P-T* conditions in ME/MEW show: K-feldspar (low Al coordination number) could be stable only below 4.5 GPa, 400 ℃ in ME/MEW fluids. Once exceeding this limit, it transforms into the assemblage containing coesite, then with pressure increasing, the transformation temperature gradually drops to 350 ℃ (8.1 GPa). The phase transition of K-feldspar to the assemblage containing coesite is irreversible and has negative Clapeyron slope. However, after the structural transition of K-feldspar into metastable structure (high Al coordination number) at above 10.3 GPa, metastable K-feldspar could remain stable even at 11.4 GPa and 400 ℃, showing a higher structural stability. Subduction zone fluids greatly affect the mineral transformation, rock melting, element mobility, and water (H_2O) is an important fluid of subduction-zone rocks. For verifying whether the higher structural stability of metastable K-feldspar still remain in the deep Earth fluids, we conducted another two high *P-T* Raman experiments using H_2O as the PTM. In H_2O, K-feldspar transformed into the assemblage containing coesite at 6.9 GPa and 350 ℃ (Figure S4 (i), Figure S6 (c)), while metastable K-feldspar could remain stable at up to 10.4 GPa and 430 ℃ (Figure S4 (j)), almost same as in ME/MEW. The decomposition of metastable K-feldspar into coesite mixture after keep in 430 ℃ for 1 h may be ascribed to the pressure change. The pressure of sample chamber decreased to 9.8 GPa because of thermal expansion and stress relief after 1 h, so the metastable phase transformed back to K-feldspar, then K-feldspar was not stable and decomposed. Therefore, metastable K-feldspar may be harder to undergo

356 metasomatism with subduction-zone fluids and can survive to deeper than previously
357 expected. In addition, the coesite mixture remain stable at 430 ℃, 9.8-10.4 GPa after
358 50 min (Figure S7), which indicates the decomposition of K-feldspar in fluid
359 composition could occur at 4.5 GPa, 400 ℃ and maintained at a certain *P-T* range
360 before the transition from K-feldspar to metastable phase. It is hard to identify
361 unambiguously the equilibrium phase(s) due to the kinetics of the phase transition.
362 But the stable existence of coesite with pressure and temperature increasing indicate
363 that the assemblage containing coesite is more stable than K-feldspar with low Al
364 coordination number at above 4.5 GPa, 400 ℃.
365
366 **Pressure-temperature phase diagram of K-feldspar**
367 The phase diagram of K-feldspar under high *P-T* conditions constrained by
368 experimental data is shown in Figure 6 along with the literature data (Lindsley 1966;
369 Zhang et al. 1993; Urakawa et al. 1994; Yagi et al. 1994; Nishiyama et al. 2005;
370 Akaogi et al. 2004; Ferroir et al. 2006; Yong et al. 2006; Hirao et al. 2008; Chen et al.
371 2019; Guo et al. 2020; Pakhomova et al. 2020). The black solid lines represent the
372 phase boundaries determined by high *P-T* experiments or from previous phase
373 diagram, the dotted lines indicate the extrapolated phase boundaries by limited data.
374 We make following changes comparing to previous studies of the phase relations of
375 K-feldspar (Urakawa et al. 1994; Sueda et al. 2004; Nishiyama et al. 2005; Yong et al.
376 2006; Hirao et al. 2008; Liu et al. 2010): First of all, this study complements the blank
377 of previous data under relatively low *P-T* conditions, and get more accurate *P-T* phase

boundaries between K-feldspar and Wd + Ky + Coe/St by Raman spectroscopy. Secondly, previous phase diagrams revealed that $KAlSi_3O_8$ with a hollandite-I and -II structures (K-holl) was stable under relatively high-pressure and low-temperature conditions. However, former studies referred to the experimental data of e.g., Nishiyama et al. (2005), in which they used K-holl-I as starting sample rather than K-feldspar. Since K-holl-I phase is quenchable, it can be detected under high-pressure, low-temperature and even ambient conditions. Combined high-pressure stability of K-feldspar in this study, the former data are not reasonable to interpret the phase behavior of K-feldspar at this *P-T* area in which K-holl phase has not formed yet. To solve this problem, three quench experiments of K-feldspar in multi-anvil apparatus were performed at 15 GPa, 500 ℃, 15 GPa, 650 ℃, and 15 GPa, 800 ℃, respectively. Raman analysis on the three quenching samples revealed the existence of K-feldspar, K-feldspar + K-holl-I, and K-holl-I (with all peaks indexed well to that in Chen et al. 2019), respectively (Figure 7). For sufficient phase equilibrium, the quench experiments at 15 GPa, 500 ℃ was kept for 12 h before rapid quenching, and the characterized result at 15 GPa, 500 ℃ indicates K-feldspar is a stable phase at below 15 GPa, 500 ℃. The coexistence of K-feldspar and K-holl-I at 15 GPa, 650 ℃ shows metastable K-feldspar is the intermediate phase between K-feldspar and K-holl-I under relatively high-pressure and low-temperature conditions. Thus, on the basis of previous phase diagram, we re-predicted the phase boundary between K-feldspar and K-holl by the results of three quenching experiments in this study, and only reserved the data of Nishiyama et al. 2005 at above the phase boundary. Finally, the phase

400 boundary between K-holl-I and K-holl-II phase was re-constrained by the data of
401 Hirao et al. (2008) in which they used K-feldspar as the starting sample.
402

403 **Implications**

404 The phase diagram of K-feldspar in the ultracold and dry subducting slab, as
405 shown in Figure 8 (a), suggests that the pressure-induced phase transition of
406 K-feldspar at relatively low-temperature (< 650 ℃) could be different from those
407 occurring at relatively high-temperature (> 650 ℃). Instead of the K-feldspar→liquid
408 / liquid + leucite in the normal or warmer mantle (> 5 ℃/km), or K-feldspar→Ky +
409 Wd + Coe/St in the ultracold subduction environments (~5 ℃/km) (Zheng and
410 Hermann 2014; Zheng 2019), K-feldspar firstly transforms into metastable phase at
411 above 10.3 GPa at relatively low-temperature. The metastable phase transition could
412 occur in extremely cold plates (<2 ℃/km, like Tonga proposed by Syracuse et al.
413 2010) at depths of ~300 km. Additionally, because the slab center is much colder than
414 the margin in some cold, old, fast, and steep slabs (Ranalli et al. 2000; Kubo et al.
415 2009; Xu et al. 2020), metastable feldspar is also likely to preserve within the center
416 of some ultracold, old, and rapidly subducting slabs. The density is similar between
417 metastable K-feldspar and the mantle at the phase transition depth (~300 km)
418 (Pakhomova et al. 2020). Thus, metastable K-feldspar has possible influence on the
419 dynamics of subducted continental lithosphere, that is, affects buoyancy, hampers
420 further subduction, and leads to a deceleration and even a potential stagnation of slabs
421 at ~300 km, just like the effects of metastable pyroxene, olivine, and plagioclase on

the slab dynamics (e.g., Hogrefe et al. 1994; Kawakatsu and Yoshioka 2011; Agrusta et al. 2014; Pakhomova et al. 2020).

The high *P-T* Raman experimental results have potential implications for the effects of subduction-zone fluids on K-feldspar. Seismic studies have shown that a amounts of water could be transported along the subducted slabs deep into the mantle (Kawakatsu and Watada 2010). Although most of the water is released from the oceanic crust at depths of 150-200 km (Iwamori 2007), under cold subduction conditions, water could be stored in hydrous minerals, or enter deeper mantle as nominally anhydrous minerals containing hydroxyl group (OH) (Wang et al. 2020). Our study indicates that K-feldspar with high Al coordination number is relatively more stable than that with low coordination number in the deep Earth enriched OH fluids (such as water). The phase relations of K-feldspar in the ultracold and hydrous subducting slab are shown in Figure 8 (b). At temperature above 350-400 ℃ subducting environments, K-feldspar with low coordination structure cannot resist fluid metamorphism and rapidly decomposes into the coesite-containing assemblage at depth above 135 km. An obvious dispersion of sample in ME/MEW/H_2O after the decomposition was observed in the experiment, so we infer low-temperature fluid metamorphism of K-feldspar may potentially affect continental slab breakoff and seismic activities. Besides, quartz is highly soluble in metamorphic fluids, so the assemblage containing coesite may be difficult to deeper subduction in metamorphic environments, which inhibits its further phase transition to form K-holl-I. Thus, the well-known phase transitions of K-feldspar→Ky + Wd + Coe/St→K-holl-I maybe

444 only occur within dry and cold slabs. However, in the subduction zones where
445 metastable phases can be preserved, K-feldspar firstly transforms into metastable
446 phase which has higher structural stability to withstand fluid metamorphism and is
447 stable at least at close to mantle transition zone, where are enriched in OH. So
448 metastable K-feldspar could survive to deeper than previously expected, and more
449 likely further subducts and transforms into K-holl-I. The phase transitions of
450 K-feldspar→metastable phase→K-holl-I could occur in both dry and hydrous slabs.
451 K-holl-I is considered to be the most abundant phase in a continental crust
452 composition in the upper and lower mantle. Studies about the existence of K-holl-I
453 was mostly carried out in a high-pressure multi-anvil apparatus, in which samples
454 were firstly compressed up to a target pressure and then heated up (e.g., Wu et al.
455 2009; Ishii et al. 2012). So the metastable phase transition process may has been
456 ignored. The phase behavior of metastable K-feldspar in ultracold subduction could
457 help us to explore the possible formation paths and conditions of K-holl-I, existing
458 depth of K-feldspar, and have further understanding of continental subduction.
459

460 **Acknowledgement**

461 We appreciate two anonymous reviewers for their constructive suggestions and
462 comments, which helped improve the manuscript significantly. This work was
463 financially supported by project of National Natural Science Foundation of China
464 (U1812402).
465

References

Agrusta, R., Van Hunen, J., and Goes, S. (2014) The effect of metastable pyroxene on the slab dynamics. Geophysical Research Letters, 41(24), 8800-8808.

Akaogi, M., Kamii, N., Kishi, A., and Kojitani, A. (2004) Calorimetric study on high-pressure transitions in $KAlSi_3O_8$. Physics and Chemistry of Minerals, 31(2), 85-91.

Aliatis, I., Lambruschi, E., Mantovani, L., Bersani, D., Andò, S., Diego Gatta, G., Gentile, P., Salvioli-Mariani, E., Prencipe, M., Tribaudino, and M., Lottici, P.P. (2015) A comparison between *ab initio* calculated and measured Raman spectrum of triclinic albite ($NaAlSi_3O_8$). Journal of Raman Spectroscopy, 46(5), 501–508.

Aliatis, I., Lambruschi, E., Mantovani, L., Bersani, D., Gatta, G.D., Tribaudino, M., and Lottici, P.P. (2017) High-pressure Raman spectroscopy on low albite. Physics and Chemistry of Minerals, 44(3), 213-220.

Allan, D.R., and Angel, R.J. (1997) A high-pressure structural study of microcline ($KAlSi_3O_8$) to 7 GPa. European Journal of Mineralogy, 9(2), 263–276.

Befus, K.S., Lin, J.F., Cisneros, M., and Fu, S. (2018) Feldspar Raman shift and application as a magmatic thermobarometer. American Mineralogist, 103(4), 600-609.

Bendel, V., and Schmidt, B.C. (2008) Raman spectroscopic characterisation of disordered alkali feldspars along the join $KAlSi_3O_8$—$NaAlSi_3O_8$: application to natural sanidine and anorthoclase. European Journal of Mineralogy, 20(6),

1055-1065.

Chen, T., Gwanmesia, G.D., Ehm, L., Le Losq, C., Neuville, D.R., Phillips, B.L., Li, B., and Liebermann, R.C. (2019) Synthesis and characterization of polycrystalline $KAlSi_3O_8$ hollandite [liebermannite]: Sound velocities vs. pressure to 13 GPa at room temperature. Comptes Rendus Geoscience, 351(2–3), 113–120.

Deng, L., Liu, X., Liu, H., and Zhang, Y. (2011) A first-principles study of the phase transition from Holl-I to Holl-II in the composition $KAlSi_3O_8$. American Mineralogist, 96(7), 974–982.

Ferroir, T., Onozawa, T., Yagi, T., Merkel, S., Miyajima, N., Nishiyama, N., Irifune, T., and Kikegawa, T. (2006) Equation of state and phase transition in $KAlSi_3O_8$ hollandite at high pressure. American Mineralogist, 91(2–3), 327–332.

Freeman, J.J., Wang, A., Kuebler, K.E., Jolliff, B.L., and Haskin, L.A. (2008) CHARACTERIZATION OF NATURAL FELDSPARS BY RAMAN SPECTROSCOPY FOR FUTURE PLANETARY EXPLORATION. The Canadian Mineralogist, 46(6), 1477-1500.

Gillet, P., Guyot, F., and Malezieux, J.M. (1989) High-pressure, high-temperature Raman spectroscopy of Ca_2GeO_4 (olivine form): some insights on anharmonicity. Physics of the Earth and Planetary Interiors, 58(2–3), 141–154.

Guo, X., Chen, S., Li, P., Zhang, Y., Wu, X., and Zhang, J. (2020) Phase transition of sanidine ($KAlSi_3O_8$) and its effect on electrical conductivity at pressures up to 11 GPa. Physics and Chemistry of Minerals, 47(4), 1–8.

Hashimoto, G.L., Roos-Serote, M., Sugita, S., Gilmore, M.S., Kamp, L.W., Carlson, R.W., and Baines, K.H. (2009) Felsic highland crust on Venus suggested by Galileo Near-Infrared Mapping Spectrometer data. Journal of Geophysical Research: Planets, 114(5), 1–10.

Henderson, C.M.B. (1979) An Elevated Temperature X-ray Study of Synthetic Disordered Na-K Alkali Feldspars. Contributions to Mineralogy and Petrology, 70(1), 71–79.

Hirao, N., Ohtani, E., Kondo, T., Sakai, T., and Kikegawa, T. (2008) Hollandite II phase in $KAlSi_3O_8$ as a potential host mineral of potassium in the Earth's lower mantle. Physics of the Earth and Planetary Interiors, 166, 97–104.

Hogrefe, A., Rubie, D. C., Sharp, T. G., and Seifert, F. (1994) Metastability of enstatite in deep subducting lithosphere. Nature, 372(6504), 351-353.

Hovis, G.L., Medford, A., Conlon, M., Tether, A., and Romanoski, A. (2010) Principles of thermal expansion in the feldspar system. American Mineralogist, 95(7), 1060–1068.

Iwamori, H. (2007) Transportation of H_2O beneath the Japan arcs and its implications for global water circulation. Chemical Geology, 239(3–4), 182–198.

Irifune, T., Ringwood, A.E., and Hibberson, W.O. (1994) Subduction of continental crust and terrigenous and pelagic sediments: an experimental study. Earth and Planetary Science Letters, 126, 351–368.

Ishii, T., Kojitani, H., and Akaogi, M. (2012) High-pressure phase transitions and subduction behavior of continental crust at pressure-temperature conditions up to

the upper part of the lower mantle. Earth and Planetary Science Letters, 357-358, 31-41.

Kawakatsu, H., and Watada, S. (2010) Seismic Evidence for Deep-Water Transportation in the Mantle. Science, 316(June), 1468-1471.

Kawakatsu, H., and Yoshioka, S. (2011) Metastable olivine wedge and deep dry cold slab beneath southwest Japan. Earth and Planetary Science Letters, 303(1-2), 1-10.

Klotz, S., Chervin, J.C., Munsch, P., and Le Marchand, G. (2009) Hydrostatic limits of 11 pressure transmitting media. Journal of Physics D: Applied Physics, 42(7).

Kubo, T., Kaneshima, S., Torii, Y., and Yoshioka, S. (2009) Seismological and experimental constraints on metastable phase transformations and rheology of the Mariana slab. Earth and Planetary Science Letters, 287(1-2), 12-23.

Lindsley, D.H. (1966). Melting relations of $KAlSi_3O_8$: effect of pressures up to 40 kilobars. American Mineralogist, 51, 1793-1799.

Liu, X., Hu Z., and Deng, L. (2010) Feldspars under conditions of high-temperature and high-pressure. Acta Petrologica Sinica, 26(12), 3641-3650.

Mao, H.K., Xu, J., and Bell, P.M. (1986) Calibration of the ruby pressure gauge to 800 kbar under quasi-hydrostatic conditions. Journal of Geophysical Research, 91(B5), 4673.

Nishiyama, N., Rapp, R.P., Irifune, T., Sanehira, T., Yamazaki, D., and Funakoshi, K.I. (2005) Stability and *P-V-T* equation of state of $KAlSi_3O_8$ -hollandite determined by in situ X-ray observations and implications for dynamics of subducted

555 continental crust material. Physics and Chemistry of Minerals, 32(8–9), 627–
556 637.

557 Pakhomova, A., Simonova, D., Koemets, I., Koemets, E., Aprilis, G., Bykov, M.,
558 Gorelova, L., Fedotenko, T., Prakapenka, V., and Dubrovinsky, L. (2020)
559 Polymorphism of feldspars above 10 GPa. Nature Communications, 11(1), 1–8.

560 Peterson, J.W., O'Meara, T.A., Seymour, M.D., Wang, W., and Gu, B. (2009) Sorption
561 mechanisms of cephapirin, a veterinary antibiotic, onto quartz and feldspar
562 minerals as detected by Raman spectroscopy. Environmental Pollution, 157(6),
563 1849-1856.

564 Ranalli, G., Pellegrini, R., and D'Offizi, S. (2000) Time dependence of negative
565 buoyancy and the subduction of continental lithosphere. Journal of Geodynamics,
566 30(5), 539–555.

567 Rogers, A.D., and Nekvasil, H. (2015) Feldspathic rocks on Mars: compositional
568 constraints from infrared spectroscopy and possible formation mechanisms.
569 Geophysical Research Letters, 42, 2619–2626.

570 Sprague, A.L., Nash, D.B., Witteborn, F.C., and Cruikshank, D.P. (1997) Mercury's
571 feldspar connection mid-ir measurements suggest plagioclase. Advances in
572 Space Research, 19, 1507–1510.

573 Sueda, Y., Irifune, T., Nishiyama, N., Rapp, R.P., Ferroir, T., Onozawa, T., Yagi, T.,
574 Merkel, S., Miyajima, N., and Funakoshi, K.I. (2004) A new high-pressure form
575 of $KAlSi_3O_8$ under lower mantle conditions. Geophysical Research Letters,
576 31(23), 1–4.

Syracuse, E.M., van Keken, P.E., and Abers, G.A. (2010) The global range of subduction zone thermal models. Physics of the Earth and Planetary Interiors, 183(1–2), 73–90.

Tseng, H., Heaney, P.J., and Onstott, T.C. (1995) Characterization of Lattice Strain Induced by Neutron Irradiation. Physics and Chemistry of Minerals, 22, 399–405.

Urakawa, S., Kondo, T., Igawa, N., Shimomura, O., and Ohno, H. (1994) Synchrotron Radiation Study on the High-Pressure and High-Temperature Phase Relations of $KAlSi_3O_8$. Physics and Chemistry of Minerals, 21(6), 387–391.

Van Mierlo, W. L., Langenhorst, F., Frost, D. J., and Rubie, D. C. (2013) Stagnation of subducting slabs in the transition zone due to slow diffusion in majoritic garnet. Nature Geoscience, 6(5), 400-403.

Wang, X., Chen, Q. F., Niu, F., Wei, S., Ning, J., Li, J., Wang, W., Buchen, J., and Liu, L. (2020) Distinct slab interfaces imaged within the mantle transition zone. Nature Geoscience, 13(12), 822-827.

Wu, Y., Fei, Y., Jin, Z., and Liu, X. (2009) The fate of subducted Upper Continental Crust: An experimental study. Earth and Planetary Science Letters, 282(1-4), 275-284.

Xie, C., Du, J., Cui, Y., Chen, Z., Zhang, W., Yi, L., and Deng, L. (2012) Variation of Raman Spectra of Oligoclase under 1.0 ~ 4.4 GPa. Spectroscopy and Spectral Analysis, 32(3), 691-694.

Xu, J., Fan, D., Zhang, D., Guo, X., Zhou, W., and Dera, P. K. (2020) Phase transition

of enstatite-ferrosilite solid solutions at high pressure and high temperature: Constraints on metastable orthopyroxene in cold subduction. Geophysical Research Letters, 47(12), 0–2.

Yagi, A., Suzuki, T., and Akaogi, M. (1994) High-Pressure Transitions in the System $KAlSi_3O_8$–$NaAlSi_3O_8$. Physics and Chemistry of Minerals, 21, 12–17.

Yamada, H., Matsui, Y., and Ito, E. (1984) Crystal-chemical characterization of $KAlSi_3O_8$ with the hollandite structure. Mineralogical Journal, 12, 29–34.

Yong, W., Dachs, E., Withers, A.C., and Essene, E.J. (2006) Heat capacity and phase equilibria of hollandite polymorph of $KAlSi_3O_8$. Physics and Chemistry of Minerals, 33(3), 167–177.

Zhang, J., Ko, J., Robert, M.H., and Charles, T.P. (1993) High-pressure crystal chemistry of $KAlSi_3O_8$ hollandite. American Mineralogist, 78, 493–499.

Zhang, R.Y., Liou, J.G., Yang, J.S., and Ye, K. (2003) Ultrahigh-pressure metamorphism in the forbidden zone: the Xugou garnet peridotite, Sulu terrane, eastern China. Journal of Metamorphic Geology, 21(6), 539–550.

Zhao, C., Li, H., Wang, Y., Jiang, J., and He, Y. (2017) SrB_4O_7:Sm^{2+}: an optical sensor reflecting non-hydrostatic pressure at high-temperature and/or high pressure in a diamond anvil cell. High Pressure Research, 37(1), 18-27.

Zheng, Y. F. (2012) Metamorphic chemical geodynamics in continental subduction zones. Chemical Geology, 328, 5–48.

Zheng, Y.F., and Hermann, J. (2014) Geochemistry of continental subduction-zone fluids. Earth, Planets and Space, 66(1), 93.

621 Zheng, Y.F. (2019) Subduction zone geochemistry. Geoscience Frontiers, 10(4),
622 1223–1254.
623

Figure Captions

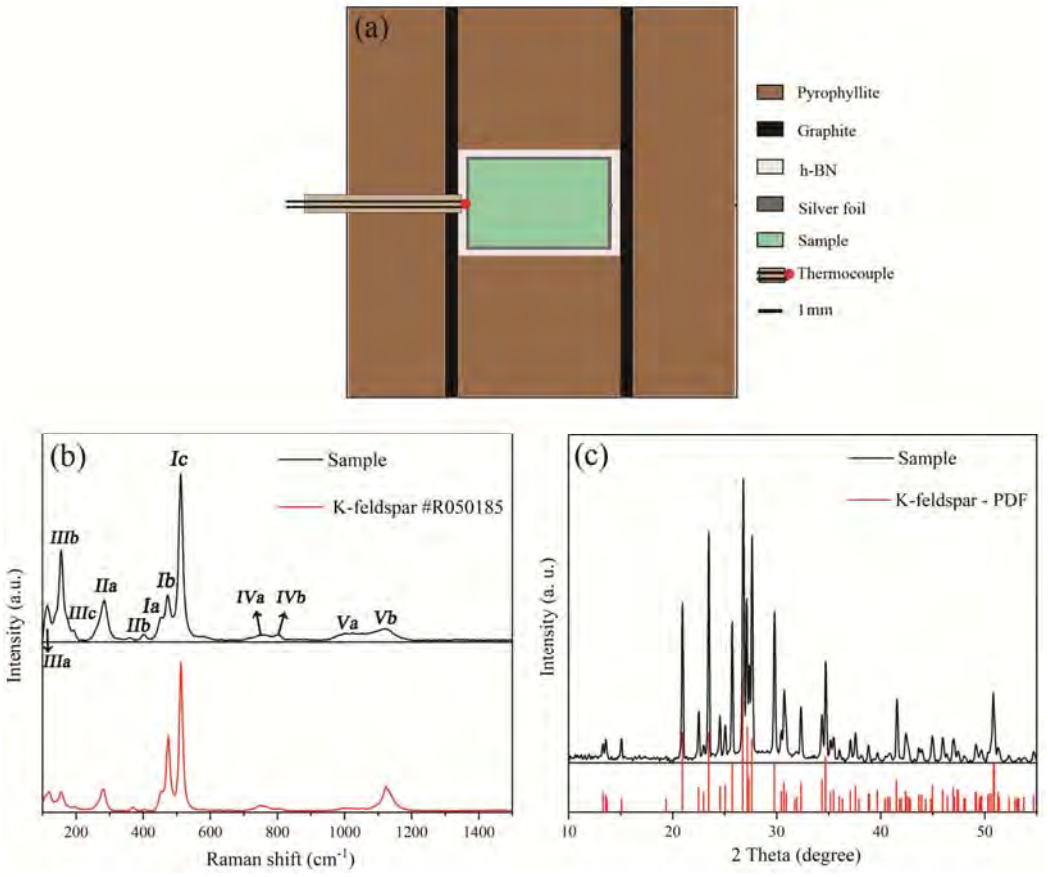

Figure 1. Schematic diagram of the sample assembly for synthesis **(a)**, sample characterization of K-feldspar by Raman spectrum **(b)** and X-ray diffraction (XRD) **(c)** under ambient conditions. The black and red solid lines represent the measured spectra and the standard spectra, respectively.

This is the peer-reviewed, final accepted version for American Mineralogist, published by the Mineralogical Society of America.
The published version is subject to change. Cite as Authors (Year) Title. American Mineralogist, in press.
DOI: https://doi.org/10.2138/am-2022-8877. http://www.minsocam.org/

640

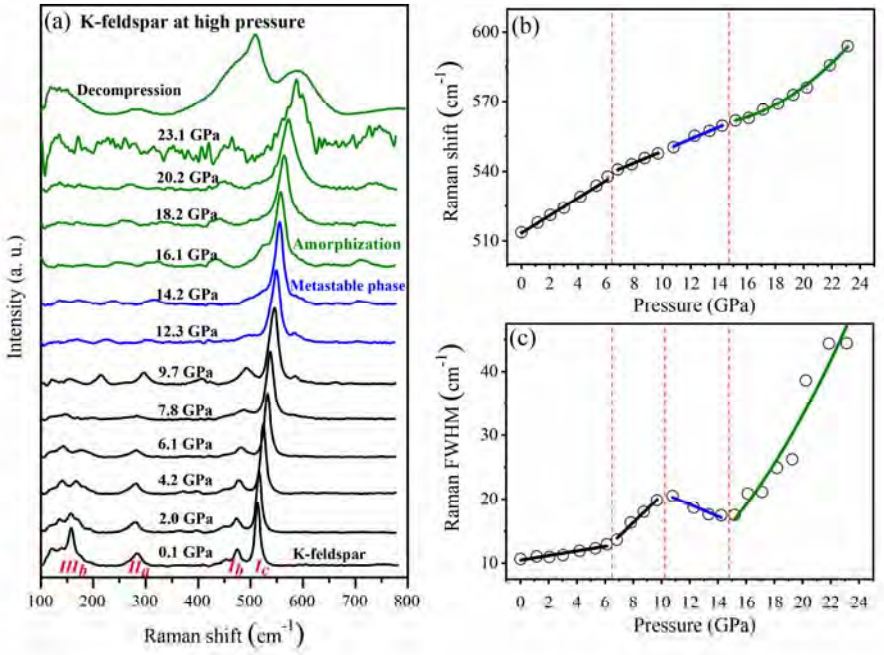

641

642 **Figure 2.** Representative Raman spectra of K-feldspar at various pressures and ambient
643 temperature, displayed in the frequency range of 100-800 cm^{-1} **(a)**, the pressure dependence of the
644 Raman shift **(b)**, and the full width at half maximum (*FWHM*) for the *Ic* mode as a function of the
645 pressure **(c)**.

646

This is the peer-reviewed, final accepted version for American Mineralogist, published by the Mineralogical Society of America.
The published version is subject to change. Cite as Authors (Year) Title. American Mineralogist, in press.
DOI: https://doi.org/10.2138/am-2022-8877. http://www.minsocam.org/

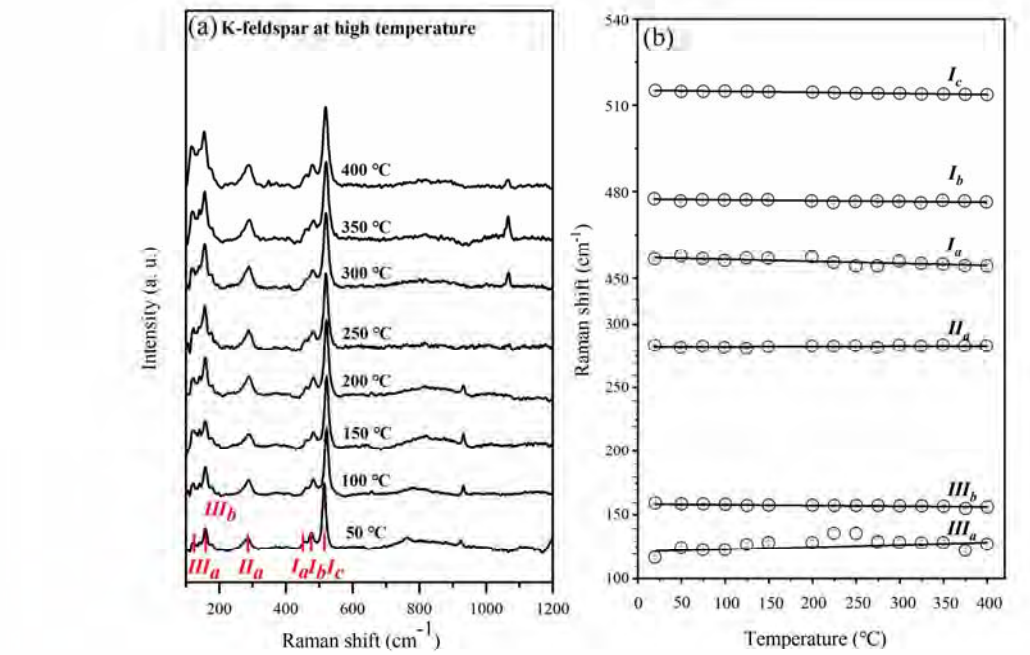

Figure 3. Representative Raman spectra of K-feldspar at various temperatures and ambient pressure, displayed in the frequency range of 100-1200 cm^{-1} **(a)**, and the temperature dependence of Raman bands of K-feldspar at ambient pressure **(b)**.

This is the peer-reviewed, final accepted version for American Mineralogist, published by the Mineralogical Society of America.
The published version is subject to change. Cite as Authors (Year) Title. American Mineralogist, in press.
DOI: https://doi.org/10.2138/am-2022-8877. http://www.minsocam.org/

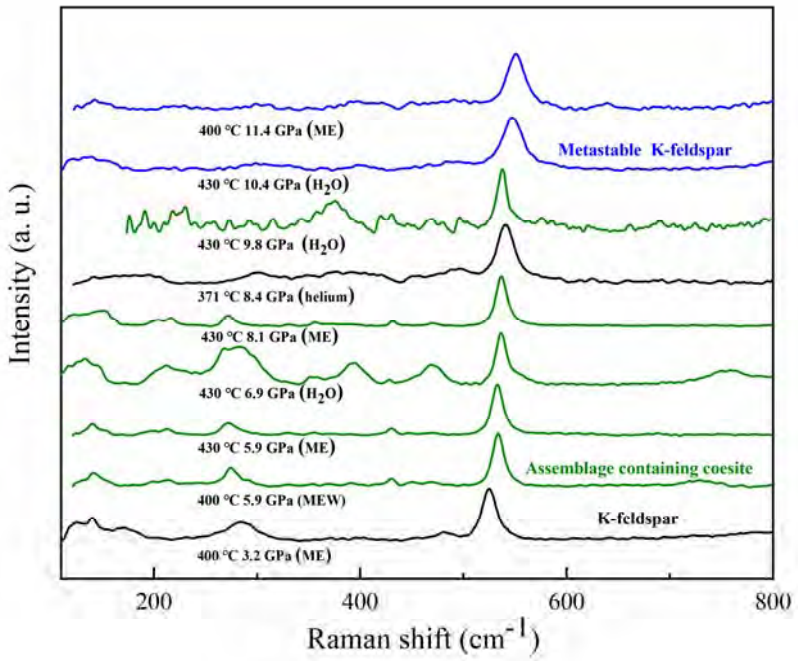

Figure 4. Representative Raman spectra of K-feldspar under different high *P-T* conditions within various PTMs (the PTMs are given in brackets), displayed in the frequency range of 100-800 cm^{-1}. The black, green, and blue solid lines represent K-feldspar, the assemblage containing coesite, and metastable K-feldspar, respectively. K-feldspar could be stable and do not decompose within the *P-T* range (0-11.4 GPa, 20-430 °C), as shown with the black and blue lines. The green and blue lines indicate K-feldspar with high Al coordination number is relatively more stable than that with low coordination number in the enriched OH fluids.

668

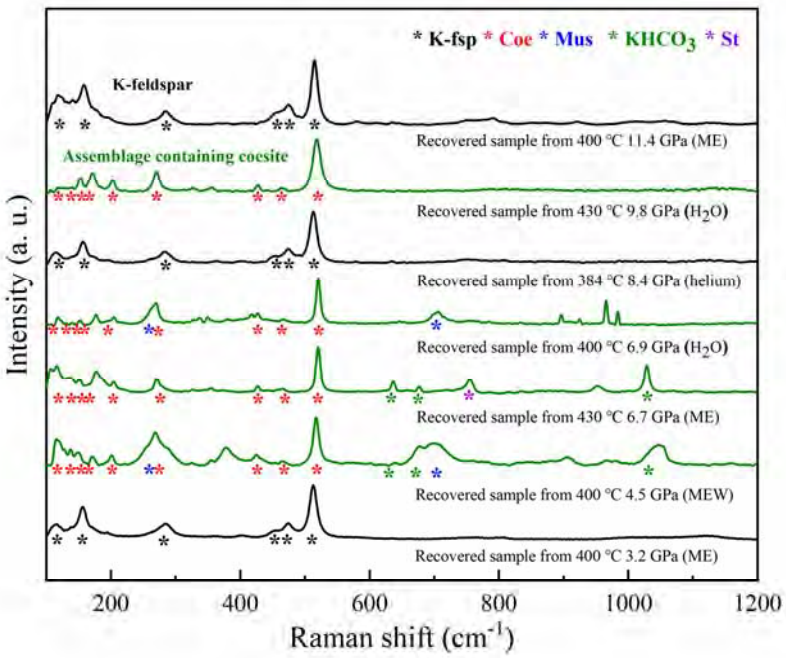

669

670 **Figure 5**. Raman spectra of samples recovered from high *P-T* to ambient conditions in different

671 PTMs (the PTMs are given in brackets), displayed in the frequency range of 100-1200 cm^{-1}. Peaks

672 with black, red, blue, green, and purple asterisk are the characteristic Raman peaks of K-feldspar

673 (K-fsp), coesite (Coe), Muscovite (Mus), $KHCO_3$, and stishovite (St), respectively. The black and

674 green solid lines represent K-feldspar and the assemblage containing coesite, respectively.

675

676

This is the peer-reviewed, final accepted version for American Mineralogist, published by the Mineralogical Society of America.
The published version is subject to change. Cite as Authors (Year) Title. American Mineralogist, in press.
DOI: https://doi.org/10.2138/am-2022-8877. http://www.minsocam.org/

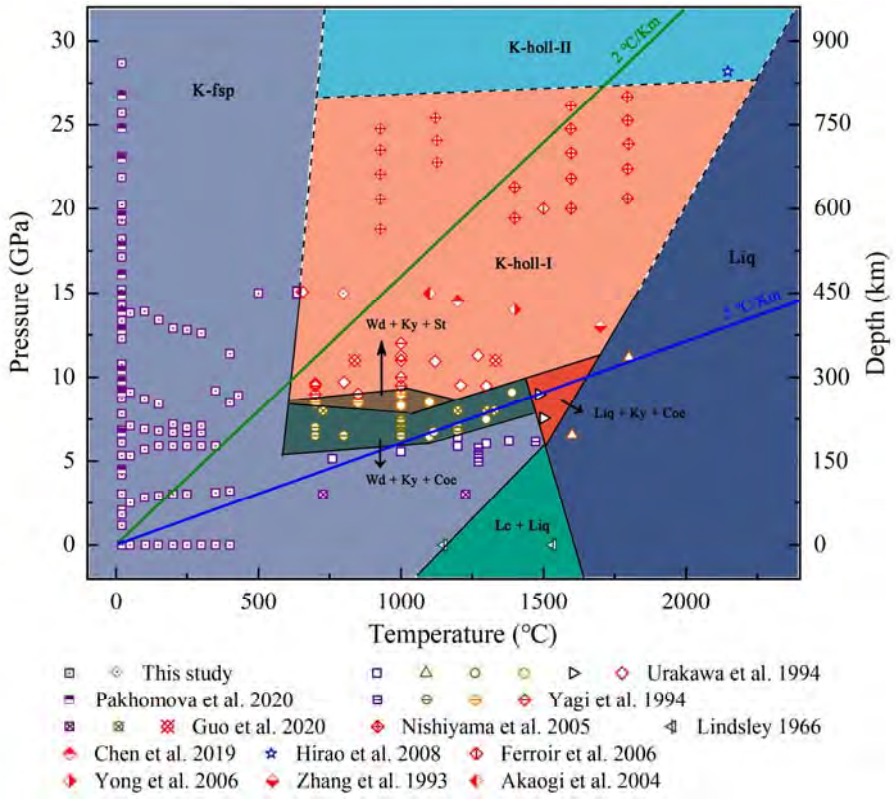

Figure 6. Phase diagram of K-feldspar constrained by high *P-T* experiments. Squares, circles, pentagon, hexagon, erected triangles, right triangles, left triangles, rhombus and stars indicate the *P-T* conditions where K-feldspar (K-fsp), wadeite + kyanite + coesite (Wd + Ky + Coe), wadeite + kyanite + stishovite (Wd + Ky + St), liquid (Liq), leucite + liquid (Lc + Liq), liquid + kyanite + coesite (Liq + Ky + Coe), hollandite (K-holl-I) and hollandite II (K-holl-II) are stable, respectively. Meanwhile, adding different colors to distinguish them more clearly. The black solid lines represent the phase boundaries determined by high *P-T* experiments or from previous phase diagram, and the dotted lines indicate the extrapolated phase boundaries by limited data (Lindsley 1966; Zhang et al. 1993; Urakawa et al. 1994; Yagi et al. 1994; Nishiyama et al. 2005; Akaogi et al. 2004; Ferroir et al. 2006; Yong et al. 2006; Hirao et al. 2008; Chen et al. 2019; Guo et al. 2020; Pakhomova et al.,2020). Green and blue lines denote the geothermal gradients at 2°C/km and 5°C/km, respectively, in subduction zones (Zheng and Hermann 2014; Zheng 2019).

This is the peer-reviewed, final accepted version for American Mineralogist, published by the Mineralogical Society of America.
The published version is subject to change. Cite as Authors (Year) Title. American Mineralogist, in press.
DOI: https://doi.org/10.2138/am-2022-8877. http://www.minsocam.org/

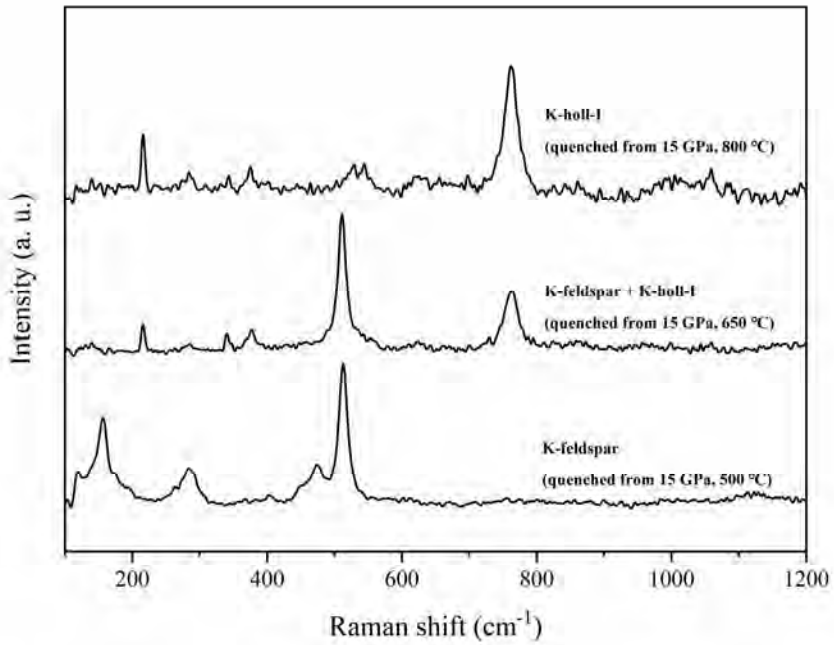

691

692 **Figure 7.** Raman spectra of samples quenched from different *P-T* conditions.

693

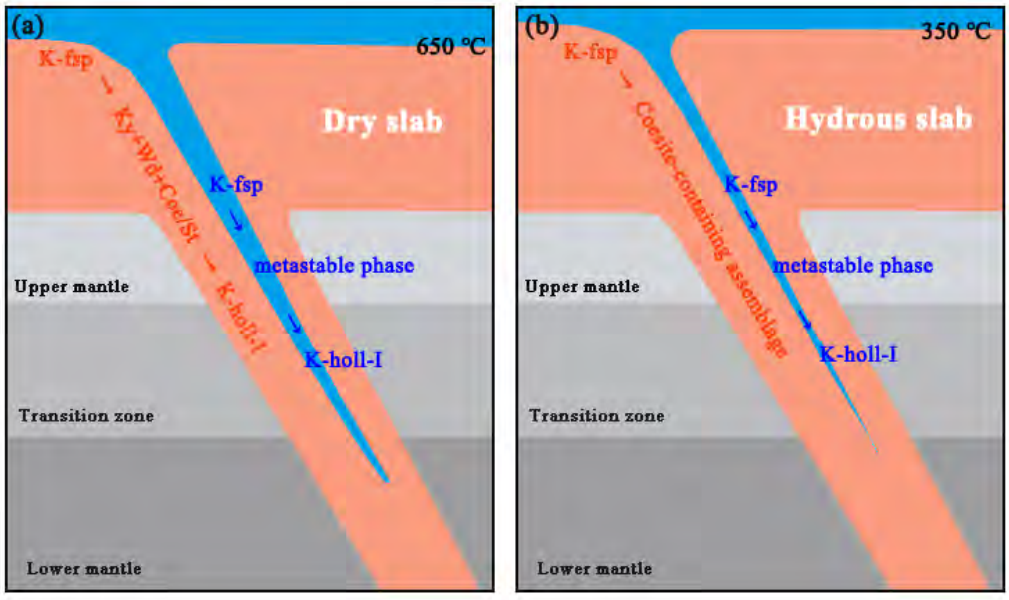

694

695 **Figure 8**. A schematic diagram of the ultracold dry **(a)** and hydrous **(b)** subducting slab and the

696 phase relations of K-feldspar. The phase transition of K-feldspar→Ky + Wd + Coe/St→K-holl-I at

697 relatively high-temperature regions (> 650 °C) is from previous studies (e.g., Zheng and Hermann

2014; Zheng 2019), while the other phase transitions (K-feldspar→metastable phase→K-holl-I, K-feldspar→Coesite-containing assemblage) are from this study. The figure is not drawn to scale. K-fsp: K-feldspar; Ky + Wd + Coe/St: kyanite + wadeite + coesite/stishovite; K-holl-I: K-hollandite-I.

Table 1. Constants determined in the expression: $v_P = v_{i0} + (\partial v_i/\partial P) \times P$, $v_T = v_{i0} + (\partial v_i/\partial T) \times T$, the isothermal ($\gamma_{iT}$) and isobaric ($\gamma_{iP}$) mode Grüneisen parameters, and the intrinsic anharmonic mode parameter (β_i) of K-feldspar.

Modes	v_{i0} (cm^{-1})	$\partial v_i/\partial P$ (cm^{-1}/GPa)	γ_{iT}	v_{i0} (cm^{-1})	$(\partial v_i/\partial T)\times10^2$ (cm^{-1}/K)	γ_{iP}	$\beta_i\times10^5$ (K^{-1})
III_a	-	-	-	124.28(13)	-0.82(3)	4.56(1)	-
III_b	157.99(13)	5.32(45)	1.96(2)	158.33(13)	-0.52(5)	2.28(2)	-0.46(2)
II_a	283.15(16)	1.41(28)	0.29(3)	284.27(16)	-0.17(1)	0.42(1)	-0.19(1)
I_a	-	-	-	455.42(10)	-0.73(6)	1.12(11)	-
I_b	474.68(10)	2.13(7)	0.26(7)	476.42(9)	-0.28(2)	0.41(5)	-0.22(3)
I_c	513.48(2)	3.56(9)	0.40(6)	515.22(2)	-0.38(1)	0.51(3)	-0.16(1)

Notes: The frequency at room pressure (v_{i0}), pressure coefficients ($\partial v_i/\partial P$), and temperature coefficients ($\partial v_i/\partial T$) obtained in this study were used to calculate the mode Grüneisen parameters (γ_{iT}, γ_{iP}) and intrinsic anharmonic mode parameter βi, using the isothermal bulk modulus (K_T) with values of 58.3(2.0) GPa (Allan and Angel 1997), and the volume thermal expansion coefficient (α) with values of $1.44(8)\times10^{-5}$ K^{-1} (Henderson 1979).

Supplementary Information

for the manuscript "A revisit to phase transition behavior of K-feldspar at high-pressure and high-temperature: Implications on metastable K-feldspar in cold subduction" by Chengcheng He et al.

Supplementary

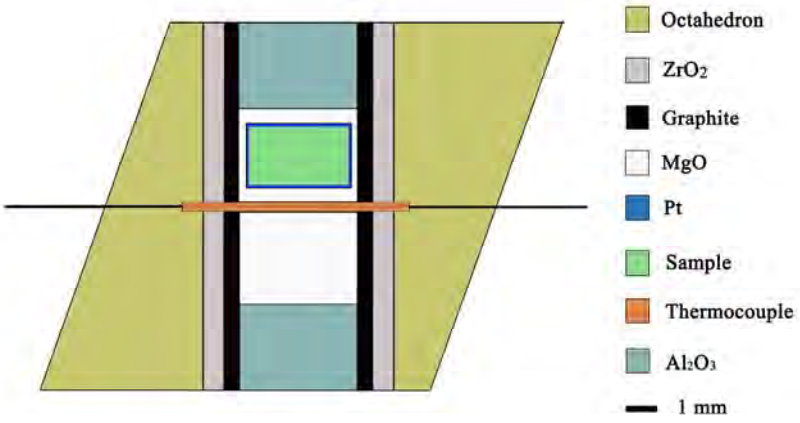

Figure S1. Schematic cross-section of cell assembly for quenching experiments.

This is the peer-reviewed, final accepted version for American Mineralogist, published by the Mineralogical Society of America.
The published version is subject to change. Cite as Authors (Year) Title. American Mineralogist, in press.
DOI: https://doi.org/10.2138/am-2022-8877. http://www.minsocam.org/

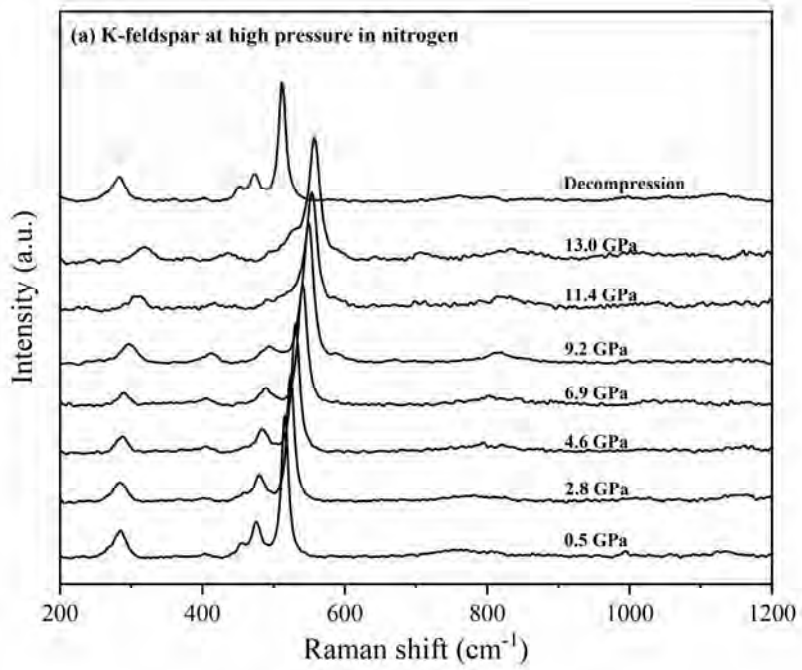

731

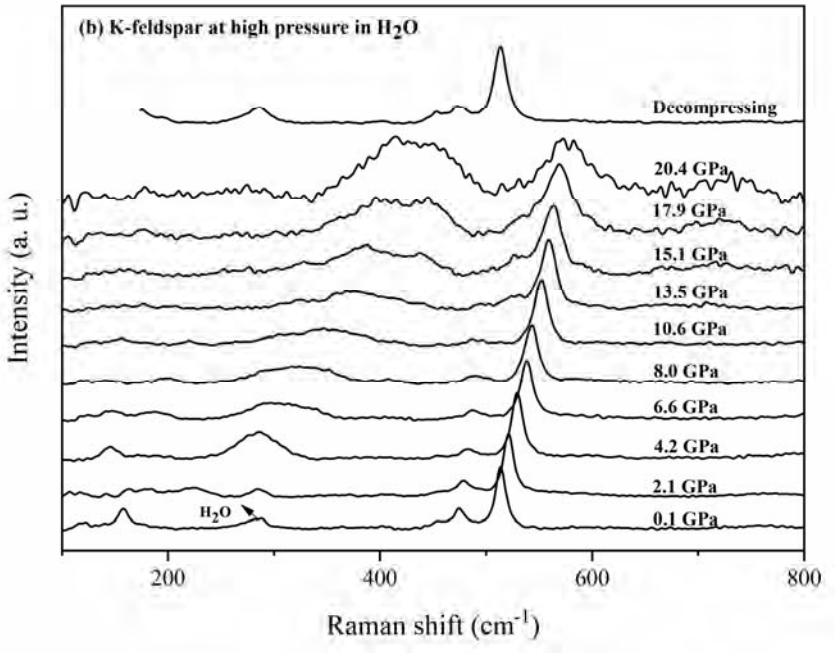

732

733 **Figure S2.** Representative Raman spectra of K-feldspar measured with increasing pressure in
734 nitrogen **(a)** and H_2O **(b)**. The decompression spectra as shown in (a) is nearly same with the
735 spectrum at ambient condition, which reveals the phase transition of K-feldspar into metastable

736 phase under high was reversible. The spectra only displayed in the frequency range of 200-1200
737 cm^{-1} because of the intense Raman bands at 100 and 200 cm^{-1} of the pressure medium nitrogen.
738 Another decompression spectra as shown in (b) is also similar with the spectrum at ambient
739 condition, which indicates the reversibility of the not fully amorphization.
740

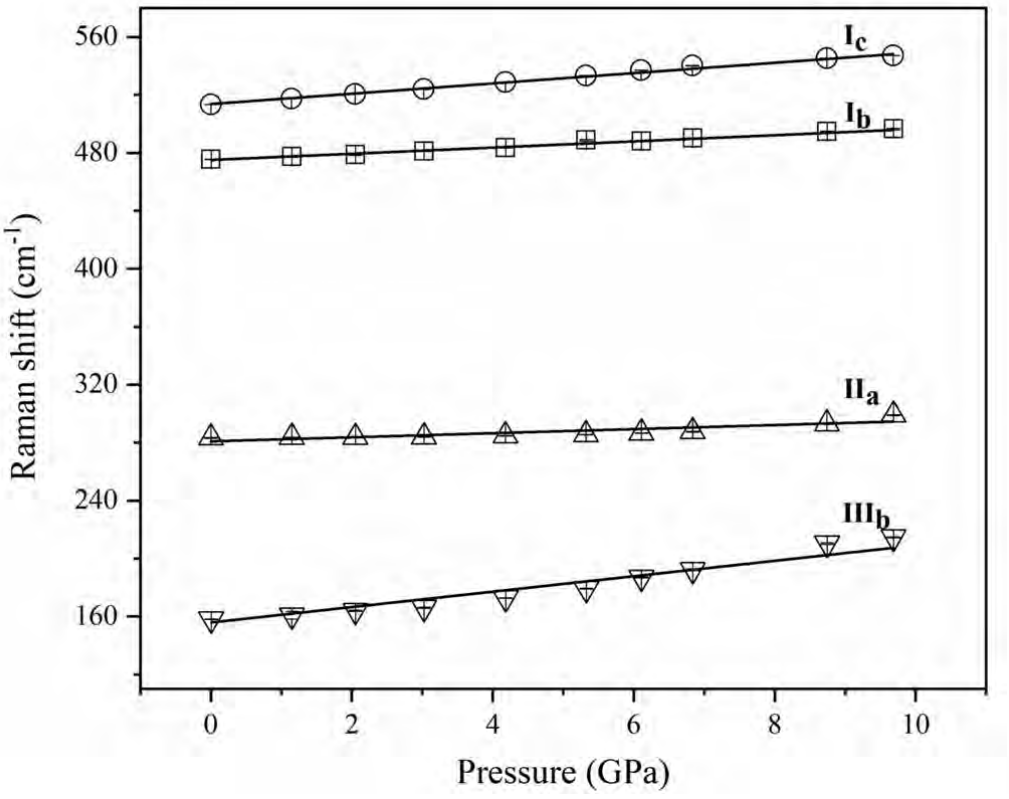

741

742 **Figure S3.** Pressure dependence of the Raman bands of K-feldspar at ambient temperature.

743

This is the peer-reviewed, final accepted version for American Mineralogist, published by the Mineralogical Society of America.
The published version is subject to change. Cite as Authors (Year) Title. American Mineralogist, in press.
DOI: https://doi.org/10.2138/am-2022-8877. http://www.minsocam.org/

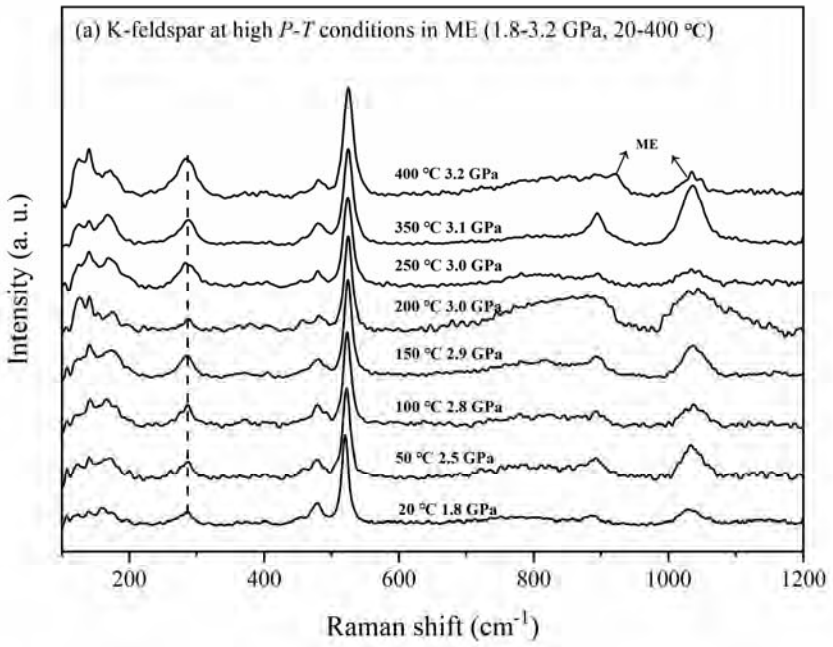

744

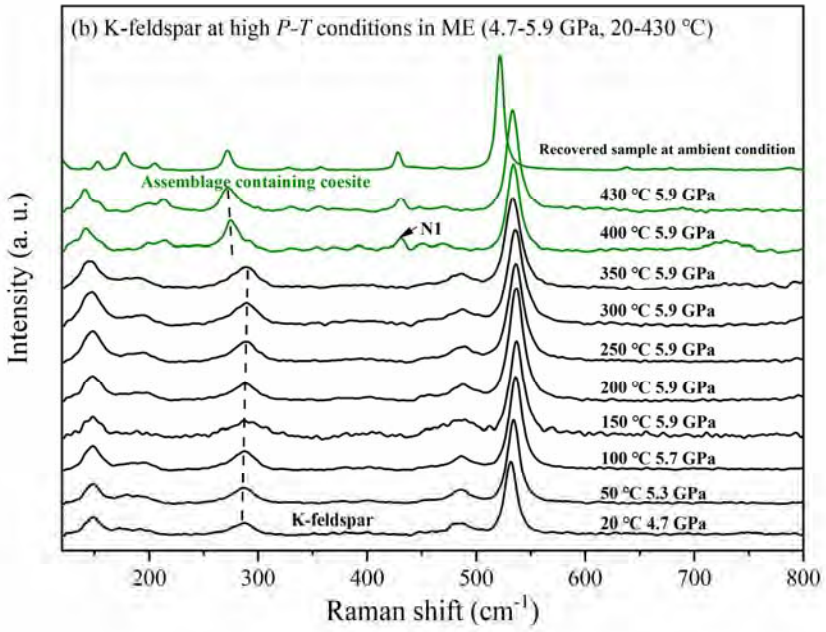

745

This is the peer-reviewed, final accepted version for American Mineralogist, published by the Mineralogical Society of America.
The published version is subject to change. Cite as Authors (Year) Title. American Mineralogist, in press.
DOI: https://doi.org/10.2138/am-2022-8877. http://www.minsocam.org/

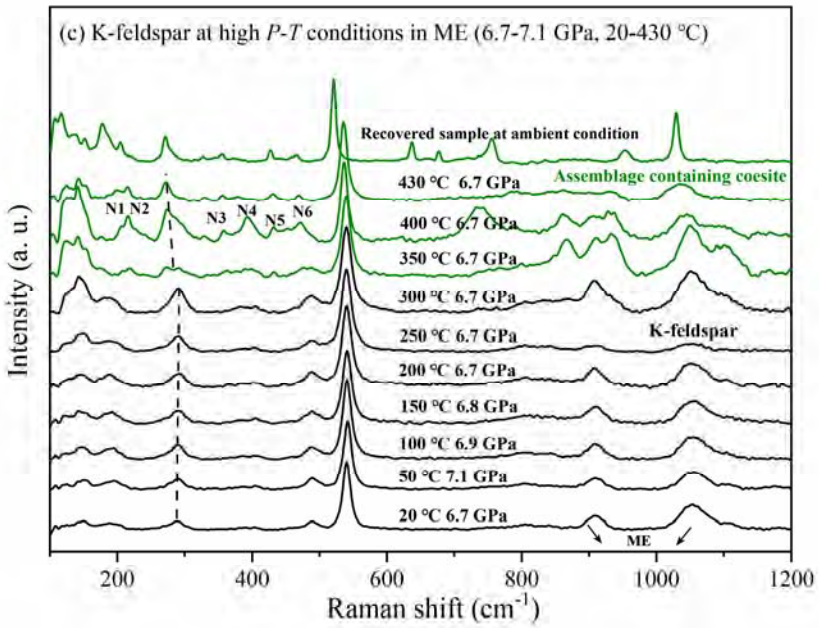

746

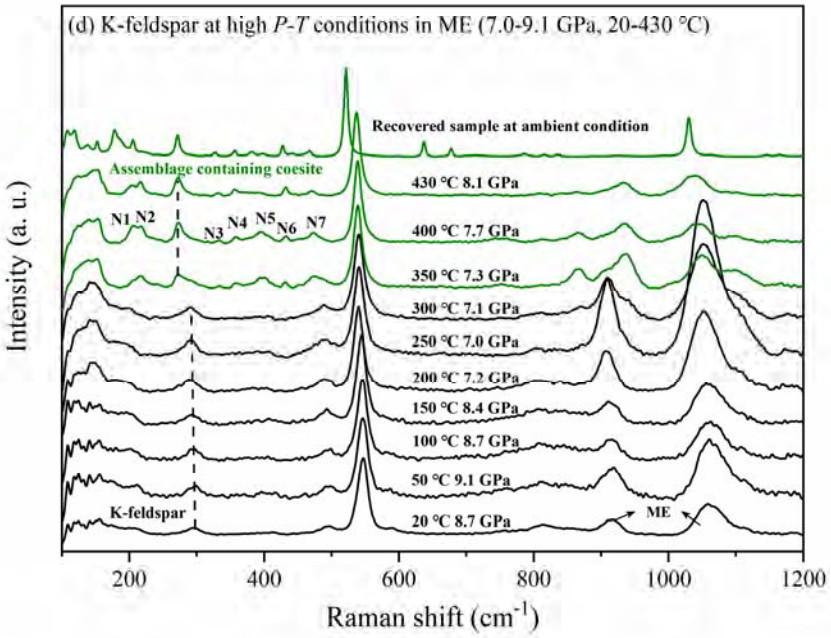

747

This is the peer-reviewed, final accepted version for American Mineralogist, published by the Mineralogical Society of America.
The published version is subject to change. Cite as Authors (Year) Title. American Mineralogist, in press.
DOI: https://doi.org/10.2138/am-2022-8877. http://www.minsocam.org/

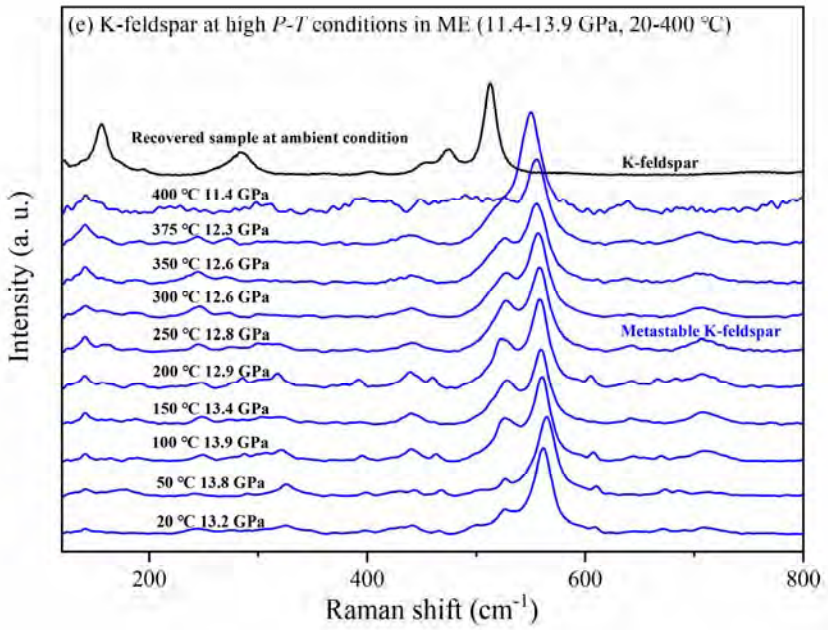

748

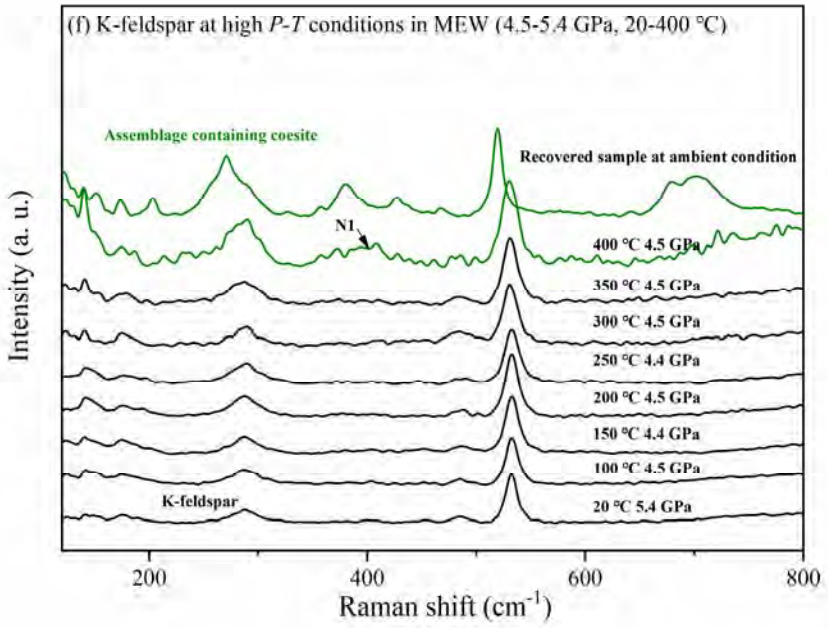

749

750

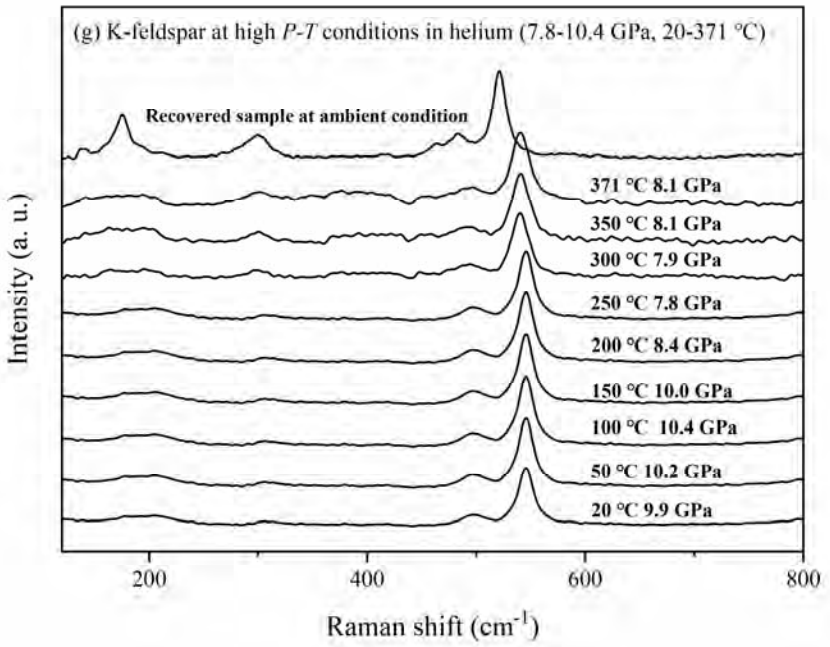

751

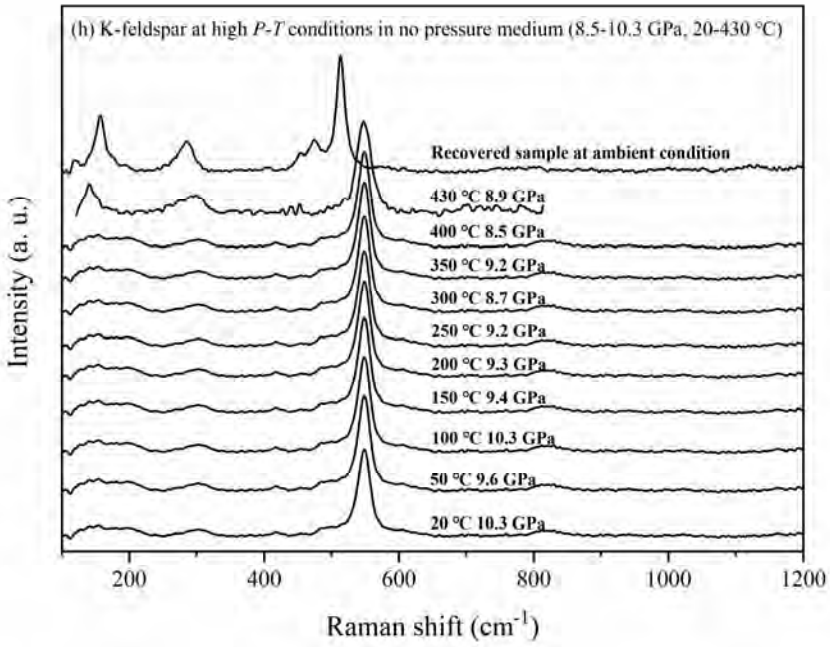

752

753

This is the peer-reviewed, final accepted version for American Mineralogist, published by the Mineralogical Society of America.
The published version is subject to change. Cite as Authors (Year) Title. American Mineralogist, in press.
DOI: https://doi.org/10.2138/am-2022-8877. http://www.minsocam.org/

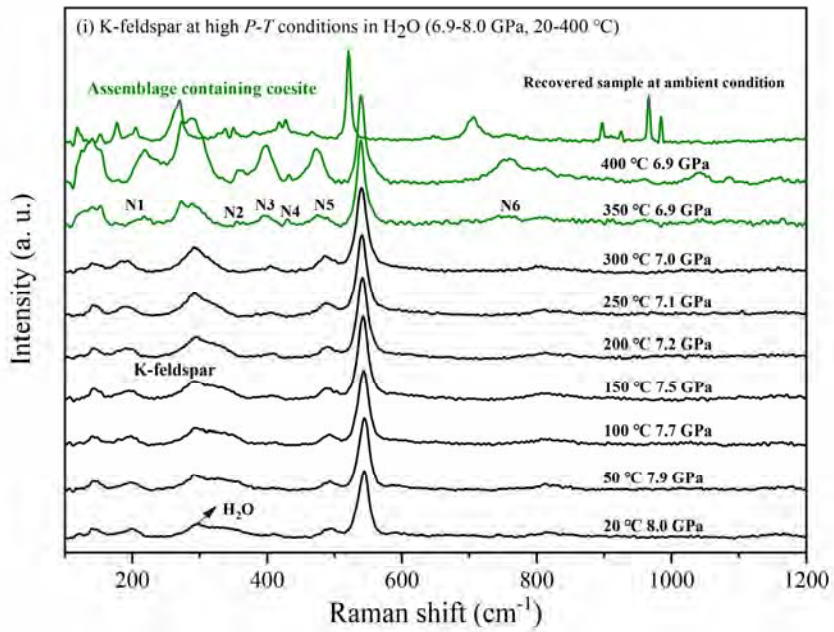

754

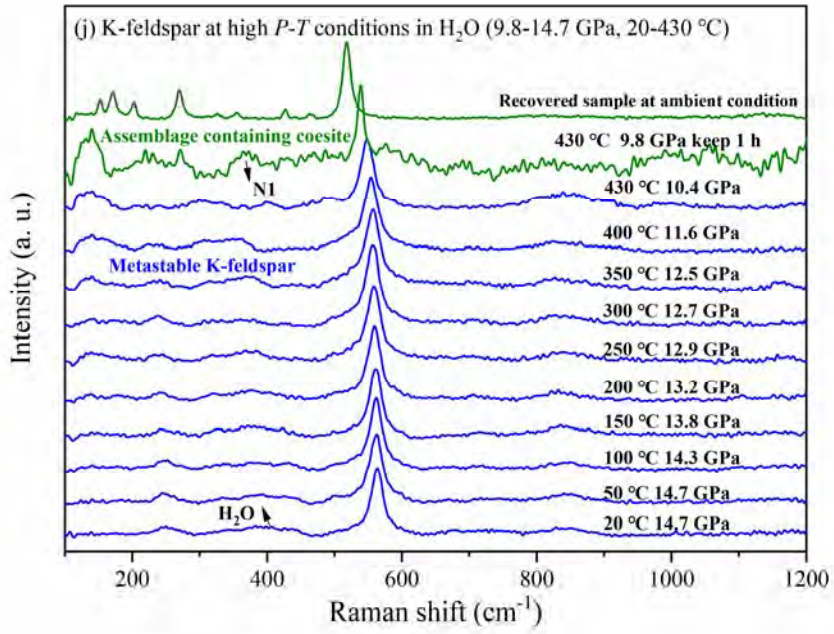

755

756 **Figure S4.** Raman spectra of the K-feldspar up to ~14.7 GPa, 430 ℃ within various PTMs.
757 Raman spectra of K-feldspar at high *P-T* in 4:1 ME mixture, 16:3:1 MEW mixture, helium, no
758 PTM, and H_2O, respectively **(a)-(e), (f), (g), (h), (i)-(j)**. N(1-7) are the new bands that may
759 correspond to the assemblage containing coesite revealed in Raman spectra of the recovered

760 samples.

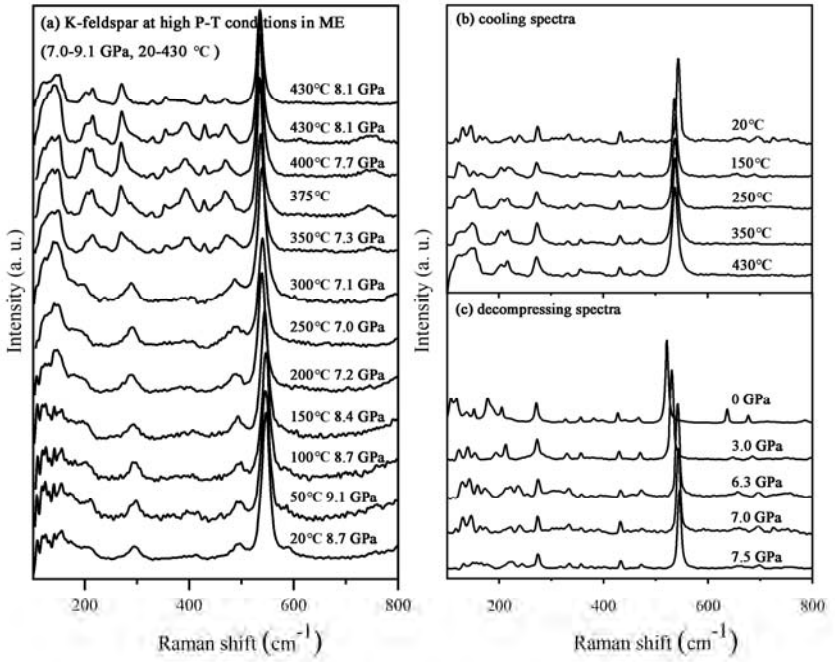

761

762 **Figure S5**. Raman spectra of K-feldspar during compressing **(a)**, cooling **(b)**, and decompressing

763 **(c)** process.

764

765

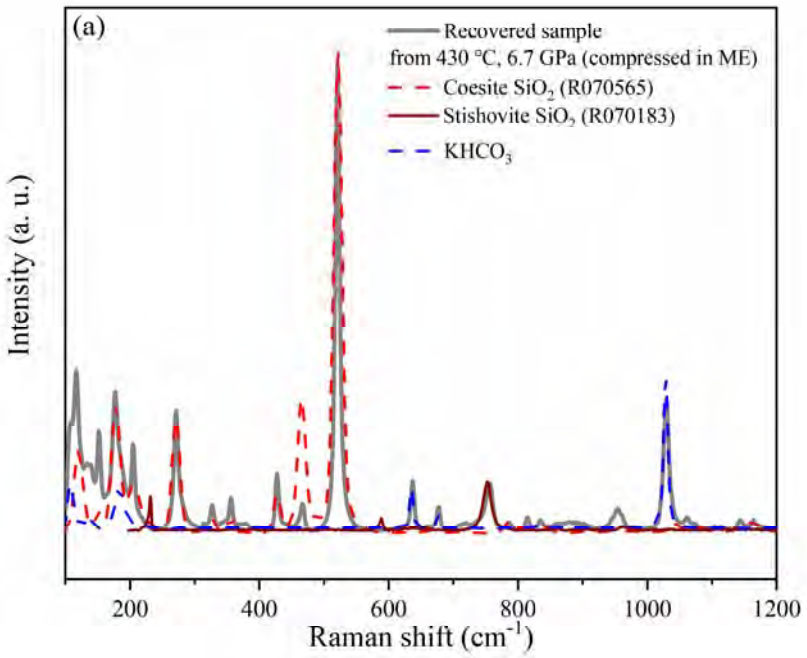

766

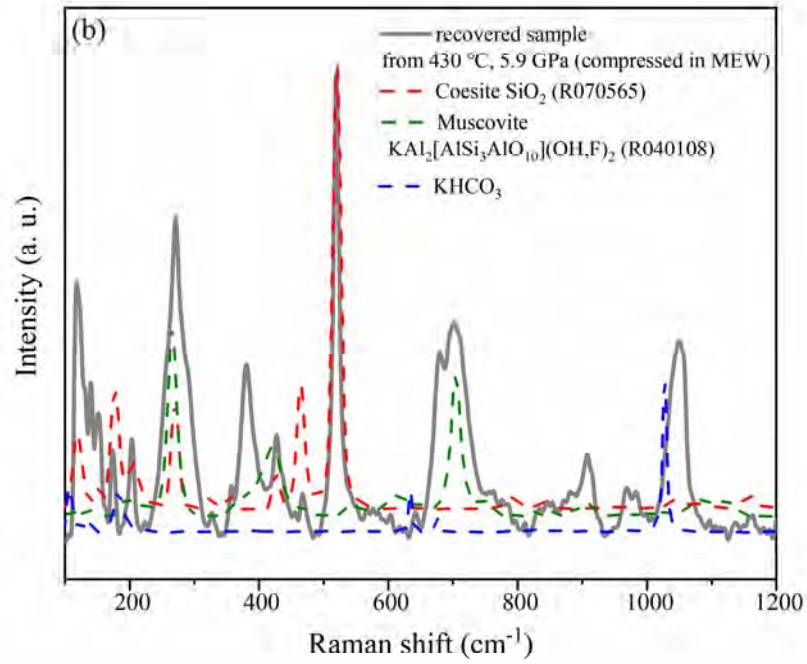

767

This is the peer-reviewed, final accepted version for American Mineralogist, published by the Mineralogical Society of America.
The published version is subject to change. Cite as Authors (Year) Title. American Mineralogist, in press.
DOI: https://doi.org/10.2138/am-2022-8877. http://www.minsocam.org/

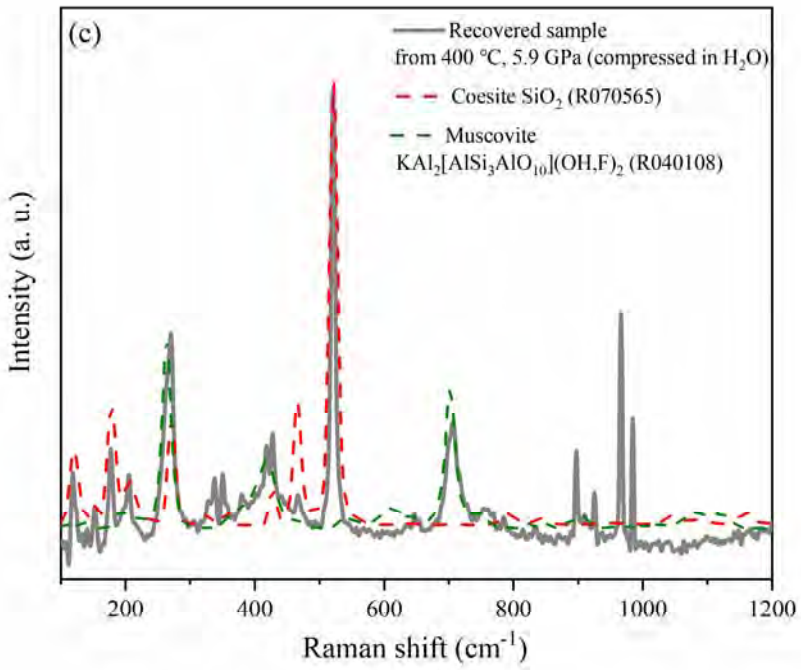

768

769 **Figure S6.** Determination of Raman spectra of recovered sample from 430 ℃, 6.7 GPa (compressed in ME) **(a),**
770 430 ℃, 5.9 GPa (compressed in MEW) **(b) and** 400 ℃, 5.9 GPa (compressed in H_2O) **(c)** by comparing with
771 standard Raman spectrum of possible substances. The standard Raman spectra of $KHCO_3$ was obtained by
772 measuring its high purity powder (99.99%, Alfa Aesar), and the others were download from RRUFF database
773 (https ://rruff .info). The recovered sample from 430 ℃, 6.7 GPa (ME) contain coesite, stishovite, and $KHCO_3$.
774 The recovered sample from 430 ℃, 5.9 GPa (MEW) contain coesite, muscovite, and $KHCO_3$. The recovered
775 sample from 400 ℃, 5.9 GPa (H_2O) contain coesite and muscovite. The possible substances corresponding to the
776 sharp peaks at 900-1100 cm^{-1} has not been determined yet, as shown in Figures (b-c).

This is the peer-reviewed, final accepted version for American Mineralogist, published by the Mineralogical Society of America.
The published version is subject to change. Cite as Authors (Year) Title. American Mineralogist, in press.
DOI: https://doi.org/10.2138/am-2022-8877. http://www.minsocam.org/

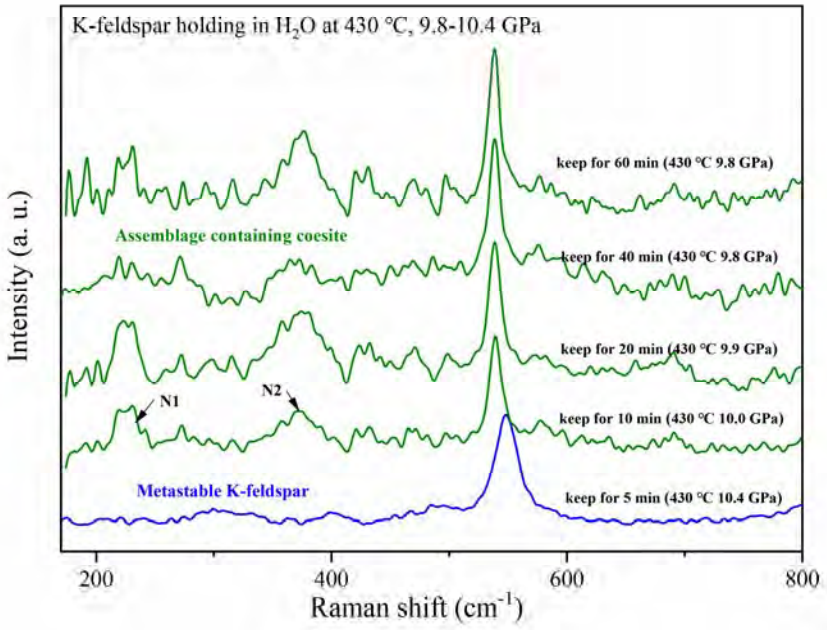

777

778 **Figure S7**. Raman spectra of K-feldspar holding at 430 °C in H_2O for 1h.

779

780